science.sciencemag.org/cgi/content/full/science.aba2412/DC1

Supplementary Materials for

Gas chromatography–mass spectrometry analyses of encapsulated stable perovskite solar cells

Lei Shi*, Martin P. Bucknall, Trevor L. Young, Meng Zhang, Long Hu, Jueming Bing,
Da Seul Lee, Jincheol Kim, Tom Wu, Noboru Takamure, David R. McKenzie,
Shujuan Huang, Martin A. Green, Anita W. Y. Ho-Baillie*

*Corresponding author. Email: anita.ho-baillie@sydney.edu.au (A.W.Y.H.-B.); lei.shi@unsw.edu.au (L.S.)

Published 21 May 2020 on *Science* First Release
DOI: 10.1126/science.aba2412

This PDF file includes:

Materials and Methods
Figs. S1 to S17
Tables S1 to S7
References

Materials and Methods

MaterialsAll chemicals were purchased from Sigma-Aldrich, Australia, Alfa Aesar, Australia, Lumtec (Luminescence Technology Corp., Taiwan) and GreatCell Solar, Australia and used without further purification except that the solvents (dimethylformamide and toluene) were dried over 4A molecular sieve. 2 mm thick FTO glass (TEC8) was also purchased from GreatCell Solar. All the solvents except IPA are ACS grade.

The PIB based polymer sealant was HelioSeal PVS101, obtained from KÖMMERLIN, Berlin, Germany. The detail of PO based polymer sealant is undisclosable at current stage as per supplier's request.

PSC fabrication

The FTO coated glass was patterned by laser scribing (FOBA M1000 pulsed ytterbium fiber laser, Alltec GmbH, Germany) and cleaned with Hellmanex solution (Sigma-Aldrich, Australia), acetone, isopropanol and UV-ozone.

A ~50 nm thick dense blocking layer of TiO_2 was deposited by spray pyrolysis of a solution of titanium diisopropoxide bis(acetylacetonate) in isopropanol (mass fraction = 8.4 %) at 450 °C.

For the fabrication of the mesoporous TiO_2 layer (mp-TiO_2), a suspension containing 150 mg/mL Dyesol 30 NR-D TiO_2 paste (GreatCell Solar, Australia) dispersed in ethanol was spin-coated at 4000 rpm (acceleration of 2000 rpm/s) for 15 s on top of the c-TiO_2 layer. The substrates were then annealed at 100 °C for 10 min followed by sintering at 500 °C for 30 min.

For the fabrication of mixed perovskite $Cs_{0.05}FA_{0.8}MA_{0.15}Pb(I_{0.85}Br_{0.15})_3$ and $FA_{0.85}MA_{0.15}Pb(I_{0.85}Br_{0.15})_3$, the appropriate amounts of CsI, FAI, PbI_2, MABr and $PbBr_2$ were mixed to achieve the desired stoichiometry and mass fraction of solution. To incorporate excess PbI_2, the quantity of PbI_2 was increased by a factor of 1.05. The solutes were dissolved in a 4:1 mixture by volume of dimethylformamide (DMF) and dimethylsulphoxide (DMSO) at room temperature. The perovskite precursor solution was spread on the mp-TiO_2/c-TiO_2/FTO and spun at 2000 rpm (acceleration of 200 rpm/s) and 6000 rpm (acceleration of 2000 rpm/s) for 10 s and 30 s, respectively, using Laurell Gbx650 (Laurell Technologies Corporation, North Wales, PA). After spinning at 6000 rpm for 10 s, the anti-solvent chlorobenzene was dispensed onto the spinning substrate for about 2 s. The films were dried on a hot plate at 100 °C to 135 °C for 20 min.

To deposit a poly[bis(4-phenyl)(2,4,6-trimethylphenyl)amine] (PTAA) HTL, A solution containing 10.0 mg PTAA, 7.5 µl of a 170 mg/mL lithium bis(trifluoromethylsulphonyl)imide solution (LiTFSI) in acetonitrile and 4.0 µl 4-tert-butylpyridine (t-BP) in 1.0 ml of toluene was spin-coated on the perovskite/c-TiO_2/FTO substrate at 3000 rpm for 30 s.

A 100 nm gold counter electrode was deposited by thermal evaporation. The Au layer was masked by either a shadow mask or Kapton-taping during deposition to create an active rectangular area of either 4.5 mm x 6 mm in diameter for small area devices used as references or 9 mm x 14 mm for large area devices that were sequentially packaged. Both positive and negative electrodes were soldered through the underlying c-TiO_2 layer for better contact and better durability during the sequential ageing tests.

While cells on small area (4.5 mm x 6 mm) typically achieve PCE's of 17 % - 19 %, cells on large area (9 mm x 10 mm) for 25 mm x 33 mm FTO glass superstrates used in this work have typical PCE's of 10 % - 13 % (Fig. S1A & B), due to the increased series resistance with area which can be circumvented by better electrode layout design (*73*) in future work.

PSC packaging

For the encapsulation of perovskite solar cells, two types of low-cost polymer sealant products were used and tested in this work: i) polyisobutylene (PIB) based polymer (PVS 101®) and ii) polyolefin (PO) based polymer. They are both excellent water barriers and low cost (Table S1).

To ensure good hermetic packaging by either blanket encapsulation or edge-seal, clean and residue free edges around the active PSC area were prepared. Edge preparation steps were performed during the PSC fabrication process. First, right before 500° C sintering of mp-TiO_2 layer, the edges of the sample were chemically wiped by ethanol, to remove the mp-TiO_2 paste and create a 5-6 mm wide uncoated margin while the centre area of 13 x 13 mm^2 was protected by an O-ring fitted metal cover from ethanol. Later, the wipe-clean step was repeated but by using Isopropanol-DMSO mixture (20:1) before the Au evaporation step to remove the perovskite / PTAA layers at the edges, resulting in a 5-6 mm wide clean margin around the active device area. The polymer sealant was then either aligned to those margins to make an edge-seal or the entire device, except the electrodes, which was finally covered with a 1-2 mm thick cover glass. Note that the Au layer is absent underneath the sealant in order to achieve optimal sealant adhesion to the substrate (c-TiO_2). The conductive path for both polarity contacts is through the FTO layer. The details of the metal-free feedthrough were described in our previous work (*25*).

After sealant application, the sample was loaded to a pre-heated (Spire 240, Spire Solar) vacuum laminator (Fig. S2A) for a two-step hot press. See Table S3 for parameters. In step 1, the background pressure was brought to below 1 mbar in less than 2 min and then wait until the desired time was reached (time started to count as soon as the sample was loaded). In step 2, the sample was pressed under certain pressure for a set time.

The encapsulation did not have detrimental effect on the PCE's of the cells (Table S4).

Characterisation

Light J-V (LJV) measurements were used to characterise the devices before the ageing tests and regularly during the ageing tests (ex-situ). When the cells were monitoring during IEC61215:2016 tests Damp Heat and Humidity Freeze tests, cells were taken out of the environmental chamber and left in ambient to "recover" for 2-4 hours as specified by the IEC61215:2016 before the LJV measurements.

The J–V measurements were performed using an ABET Sun 3000 solar cell I–V testing system from PV Measurements, Inc. (using a Keithley 2460 source meter) under an illumination power of 100 mW/cm^2 (calibrated by RS-ID4 reference solar cell, FHG-ISE) with an 0.159 cm^2 aperture. During the J-V measurement, the aperture was placed in the same position (centre of the active area) for all cells. All J-V measurements were made under room ambient conditions. The temperature of the sample was maintained between 25 ^{0}C and 30 ^{0}C. The cell was preconditioned by illuminating at 100 mW/cm^2 for 5 s right before the current was measured as the voltage was scanned from 1.2 V to -0.1 V (reverse scan) or from -0.1 V to 1.2 V (forward scan) at 100 mV/s, with 3 ms dwell time. The average V_{OC}, J_{SC}, FF and R_S were obtained and reported from LJV scans in the two opposite directions (1.2 V → -0.1 V or -0.1 V → 1.2 V) (*25*). PCE reported is the average of the PCE's obtained from two scan directions. This PCE reporting method is reliable when compared to another commonly used "stabilised" method whereby the stabilised PCE is obtained by measuring the current at the voltage corresponding to the maximum power point (V_{MPP}) until the current stabilised under light soaking (*74*). Table S5 shows that there is negligible difference between PCE's obtained using the averaging method and the stabilised method, which holds for the case of a fresh cell and a thermally degraded cell. Therefore, the averaging method is used in this work as it is less time consuming (less exposure of a bare cell to the LJV test condition), and it allows for reporting of J_{SC}, V_{OC}, FF and R_S (averaged from the two scans) which the stabilised method does not provide. Maximum power point tracking (MPPT) testing per standard algorithm was carried out in a Steridium customised weathering chamber (Fig. S2C) under controlled environment (AM1.5G, 1 sun, 25 – 45 °C, 30-50 %RH).

X-ray diffraction (XRD) measurements were performed on a PANalytical Xpert Materials Research diffractometer system with a Cu Kα radiation source (λ = 0.1541 nm) at 45 kV and 40 mA.

Photoluminescence (PL) spectra were measured using a back-scattering geometry with laser excitation of 405 nm and a thermo-electrically cooled Si-CCD detector. The detector temperature is -60 °C and exposure time is 100 ms.

Headspace GC-MS sample preparation

The sample was first loaded into a glass headspace vials in an N_2-filled glovebox. Two vial types were used: 20 mL 'tall' vials for powdered precursor materials (75 mm high x 23 mm dia., from Thermo Scientific) or 10 mL 'short' Vials for other samples (46 mm high x 23 mm dia., Verex Brand, from Phenomenex). Vials was crimp-sealed with an aluminium cap which had a PTFE/Silicone septum embedded (Verex seal 20 mm dia., from Phenomenex).

Sample preparation of perovskite precursor powders, perovskite films, cells, PTAA films and standard gases

Powders

Dry MAI, FAI, MABr and $(FAI)_{0.85}$ + $(MABr)_{0.15}$ powders were loaded separately in four 20 mL glass Headspace vials with 100 or 500 mg in each vial with all the powder grains sitting at the bottom of the vial. Vials were annealed on a hotplate at 350 °C for 15 min. The top end of the vial was not heated to more than 80 °C. The powder grains were placed evenly at the bottom of the vial, piling up to less than 2 mm height. After annealing, the vials were then left cool to room temperature on the hotplate and were sequentially loaded onto the headspace GC-MS autosampler for analysis.

Cells and PTAA films

The perovskite film deposition processes were the same as described in the "PSC fabrication" section except that i) samples with structure Con. 1-3 had their edges taped during the perovskite and PTAA spin-coating steps; ii) samples were cleaved to the size of 1 x 2 mm^2 after Au evaporation so that they could fit inside the HS vials (except for the cases where cells were manually sampled to assess their internal gas volumes). For samples with PIB or PO sealants, the materials around the edges were scraped and chemically wiped to create a margin of 1.5 mm wide. The encapsulation step was the same as described in section "PSC packaging". All the thin-film samples were sealed in glass vials in a N_2 filled glove box. The vials were baked in an oven at 85 °C for 100 h to generate any possible outgassing. After naturally cooling to room temperature, the vials were loaded onto the HS GC-MS autosampler for GC-MS analysis.

For manual sampling and injection, the fabrication procedure of PIB edge sealed thin-film samples is as described in section "PSC fabrication" and "PSC packaging" except that a 1 mm void was created between the sample surface and the cover glass by placing two glass spacers (dimension L10 mm, W1 mm, H1 mm) under the cover glass before the lamination step. This modification facilitated manual sampling of the gaseous substances in the void using a 500 uL glass headspace syringe. The active area was kept approximately the same for all other thin-film samples. The samples were baked in in an oven at 85 °C for 100 h to generate any possible outgassing before being naturally cooled to room temperature for GC-MS analysis. Immediately before the manual sampling, the edge sealed samples and the headspace syringe (HS syringe with valve, SGE 500R-V-GT, SGE, Clayton, Victoria, Australia) were heated to 40 °C for easier penetration through the PIB sealant. The syringe was pre-filled with 0.2 ml N_2 prior to penetration of the PIB sealant. The N_2 was injected into the void and then 0.4 ml of the gas from the void was drawn back into the syringe. The syringe valve was closed to prevent leaking before the needle was retracted from the void. When sampling a CsFAMA PSC, the PIB maintained a reasonable seal throughout the sampling course as evidenced by the plunger spontaneous movement due to the pressure difference between the void and the atmosphere. However, the seal was not successfully maintained when sampling a FAMA PSC. The sampled gas was immediately injected into the GC-MS PTV inlet for analysis.

Standard gases CH_3NH_2, CH_3I, CH_3CN, HI and NH_3

The identification of key decomposition products was verified by GC-MS measurement (except for HI which was verified by Direct MS analysis as described below) (Fig. S4A to D) of the following same commercially available standard gases. For this work, we did not purchase formally certified reference materials (CRM's) but used reagent grade chemicals to synthesize gases using well-established reactions. We refer to these in-house produced gases as 'standards' whist recognizing that they were not CRM's.

For CH_3NH_2 (methylamine) gas preparation, 33 wt.% methylamine (in ethanol) solution was added into a 10 mL glass vial containing DMSO to make a final solution with 1 µL/mL concentration. The vial was sealed in ambient atmosphere.

For CH_3I (methyl iodide) gas preparation, 5 µL CH_3I liquid was sealed in a 10 mL glass vial. To avoid overloading the mass spectrometer, CH_3I gas was diluted by 20 times using a syringe to extract 500 uL gas from the original vial immediately after it was baked at 85 °C for 2 minutes and inject into another N_2 filled and sealed 10 mL glass vial.

For CH_3CN (acetonitrile) gas preparation, the procedure was the same as CH_3I gas preparation.

For HI gas preparation, 20 µL hydroiodic acid solution with concentration of 57 wt.% (in water, no stabilizer) was added into a 20 mL glass vial containing 2 g phosphorus pentoxide for dehydration. The vial was sealed immediately after the bubbling (confirming that hydroiodic acid had been successfully dehydrated to HI gas).

For NH_3 (ammonia) gas preparation, 500uL of NH_4OH is placed in 16 mL plastic syringe immersed in water bath at 70 °C. Evolved gas was sampled using a 500 uL of glass head space syringe injected into a N_2 containing vial followed by analysis.

All the above preparation procedures were conducted in a N_2 filled glovebox except that CH_3NH_2 gas was prepared in room atmosphere. Gas dilution procedures were also performed in an ambient room atmosphere using nitrogen containing vials that had previously been sealed inside the N_2 glovebox.

Some other standard gases of interest, such as HCN, CH_3Br, $H_3C_3N_3$, were not conveniently available due to the laboratory safety restrictions or chemical supply issues and hence not measured for this verification purpose.

Headspace GC-MS analytical methods (QPlot method and Amine method)

Gas chromatography (GC) was used to separate the components in a mixture and in this work, was used in-line with mass spectrometry (MS), to identify and quantify gas components at a high level of sensitivity and specificity. Automated headspace gas chromatography – mass spectrometry (GC-MS) analysis was performed using a Thermo

TriPlus Headspace (HS) autosampler interfaced with a Thermo Trace DSQ II Quadrupole GC-MS (Thermo Scientific, Watham, MA) (Fig. S3).

Samples placed in the headspace autosampler tray were incubated sequentially (detailed in the methods below) before the sealed gas was sampled by a heated glass 2.5 mL purgeable autosampler syringe. The syringe needle penetrated the PTFE/Silicone septum vial seals. A volume of Helium gas, equal to the amount to be withdrawn, was pre-filled into the vial to balance the pressure inside. The sample volume was then withdrawn into the hot syringe. The septum was thick enough to reseal and prevent leakage through the septum puncture so that the remaining gas in the vial was uncontaminated by ambient air and could be re-sampled.

The sampled gas volume was injected into the programmable temperature vaporizer (PTV) inlet of the Trace GC, which was equipped with a Merlin Microseal mechanical septum (Supelco, Bellefonte, PA) and a 1 mm internal diameter glass inlet liner, operated at an elevated temperature in constant temperature split mode at a certain split ratio. Either a Restek Rt-QPLOT column (30 m x 0.32 mm) or Restek Rtx-VolatileAmine column (30 m x 0.32 mm) (both supplied by Leco Australia Pty., Castle Hill, NSW Australia) was connected to the PTV inlet. The helium carrier gas was set to a constant flow, detailed in the methods below, and oven equilibration time to 1 minute. The heated syringe was constantly purged with helium between runs and the 'pre-filling' parameter was enabled.

The mass spectrometer was operated in electron impact ionization (EI+) mode, either scanning the range *m/z* 14-400 (for identification) or using the single ion monitoring (SIM) parameters listed in the corresponding Tables S6-S7 below (for quantification). The detector gain was set to a value of 3×10^5. The chromatographic peaks were identified by comparison with reference spectra from the NIST 2011 / Wiley 9 Combined Mass Spectral Library, using the NIST Mass Spectral Search program, version 2.0g. Spectral matching scores exceeding 900/999 were indicative of a positive compound identification.

SIM chromatograms for the quantitation ions were smoothed (7-point Gaussian) and integrated in Thermo Qual Browser software (Version 2.1.0.1140) using the following parameters for NH_3: Baseline Window 30, Area Noise Factor 3, Peak Noise Factor 25 and Multiplet Resolution 2. Parameters for other analytes were: Baseline Window 40-60, Area Noise Factor 5-10, Peak Noise Factor 30-50 and Multiplet Resolution 10. All other integration parameters were set to default values. The area of the SIM chromatographic peak for each analyte was recorded.

The GC oven temperature profiles and other GC-MS parameters for the Qplot and Amine methods are collated in Tables S6 & S7.

Direct MS analysis (fused silica gas introduction) method

For investigating the production of hydrogen iodide (HI) (Fig. S12, S13 and S17E)) which is known to react with GC column stationary phases designed for organic molecules, and accordingly provides GC-MS results with poor reproducibility, headspace gases were directly introduced into the mass spectrometer. This prevented chromatographic separation of the analytes, but also avoided reaction of any produced HI with the column stationary phase.

A 2.5 m length of 100 µm internal diameter, 360 µm external diameter fused silica tubing (Polymicro Technologies, a division of Molex), was inserted into the GC interface / transfer line of the MS system, in lieu of the GC column and coiled inside the GC oven with approximately 80 cm protruding from the GC door seal. This free end of the fused silica was connected to a 22 Gauge, cone-tipped stainless-steel needle via an Upchurch M-560 Precolumn Microfilter 0.5 µm (Idex Health and Science LLC, Oak Harbor, WA). The filter union prevented clogging of the fused silica by particles in the headspace gas or by dust in ambient air that might flow into the fused silica. Sample gases and/or ambient air were drawn through the 22-gauge needle into the system by the MS vacuum at a flow rate calculated to be 0.11 mL/min. The GC oven was maintained at 100 °C and GC interface at 120 °C. Although the autosampler and PTV inlet of the system were not active in this configuration, the headspace heater block was maintained at 85 °C and used to manually warm the sample vials. The MS scanned *m/z* 60-270 at a rate of 2.5 scans per second. In order to protect the filament from excessive oxidation by ambient air, the electron current was reduced to 50 μA. The detector gain was also reduced relative to the GC-MS experiments, and set to a value of 0.5×10^5 to protect the detector from saturation-level ion currents.

Analytical runs were manually activated. The MS was set to begin with continuously acquiring ambient air spectra, then a pre-warmed nitrogen-filled vial (as an analytical blank), and finally a pre-warmed sample vial, for approximately 4 minutes for each gas source. The vials were sampled by manually forcing the 22-gauge needle through the septum seals of the headspace vials whist after they were pre-warmed by the 85 °C heater block.

Sample mass spectra were averaged, and averaged background or blank spectra were subtracted to provide mass spectra for comparison with standard HI mass spectra. HI is not contained in the NIST 2011 / Wiley 9 Library of Mass Spectra, so standard HI was prepared from hydroiodic acid liquid as detailed above. This gas was diluted in nitrogen and then analysed in the same way as the samples, in order to obtain a reference mass spectrum for HI.

The resulting mass spectrum featured a molecular ion at m/z 128 for HI, along with the usual ions seen in library mass spectra of iodine. These are a low intensity m/z 63.5 (I^{++}), along with higher intensity 127 (I^+) and 254 (I_2^+). The relative intensities of these ions appear to vary with the HI concentration entering the MS (Fig. S17E). The suggestion is that HI is largely converted into iodine by electron bombardment in the ion source, although the mass spectra always differ from those of pure iodine by the presence of an m/z 128 peak of comparable height to m/z 127.

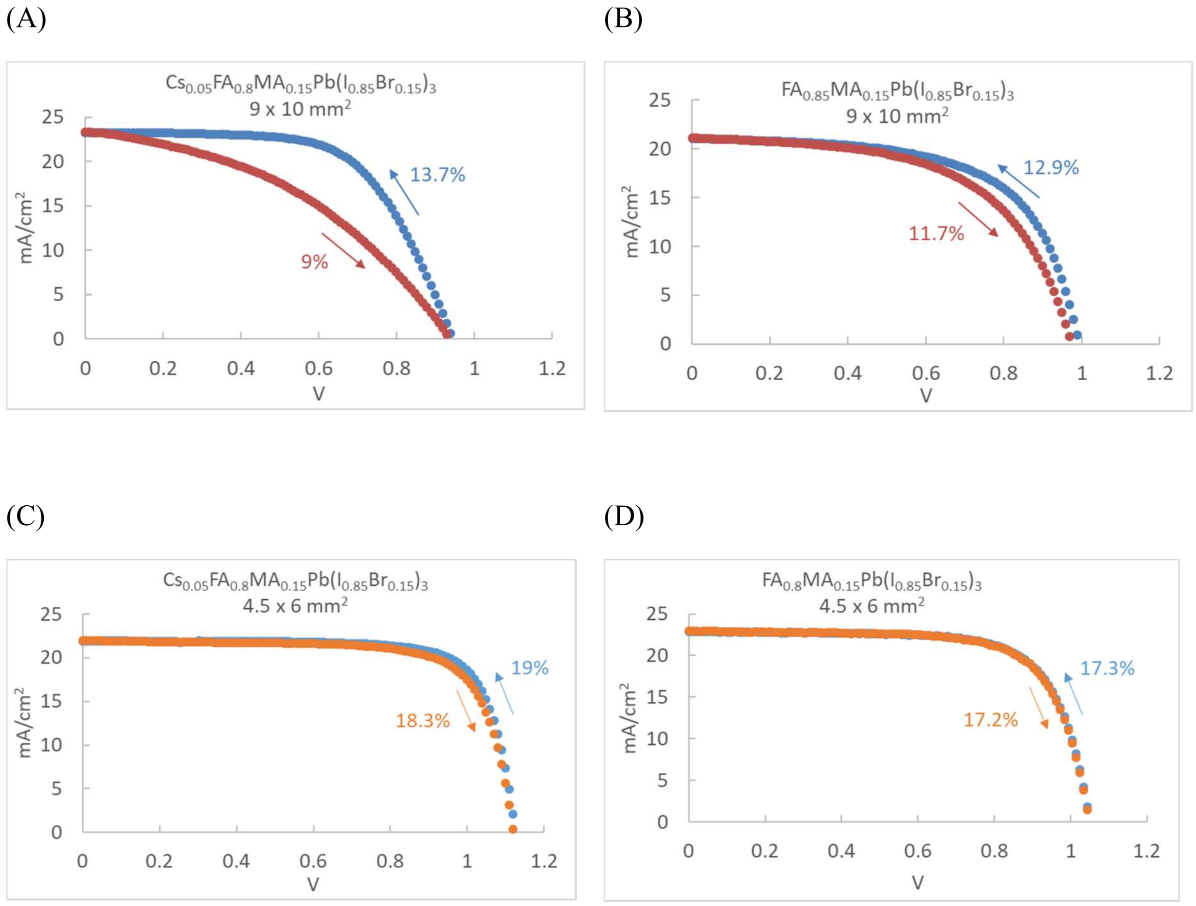

Fig. S1.

LJV curves under reverse and forward scans at 100 mV/s and the corresponding PCE's of typical (A, C) $Cs_{0.05}FA_{0.8}MA_{0.15}Pb(I_{0.85}Br_{0.15})_3$ and (B, D) $FA_{0.85}MA_{0.15}Pb(I_{0.85}Br_{0.15})_3$ cells on (A, B) 9 x 10 mm^2 active area (for packaging and accelerated lifetime testing) and (C, D) 4.5 x 6 mm^2 active area (for efficiency demonstration).

Fig. S2.

The equipment for (A) Spire 240 vacuum lamination for encapsulation; (B) Espec SMS-2 environmental chamber for IEC Damp Heat and Humidity Freeze testing. (c) Steridium (customised) weathering chamber for MPPT

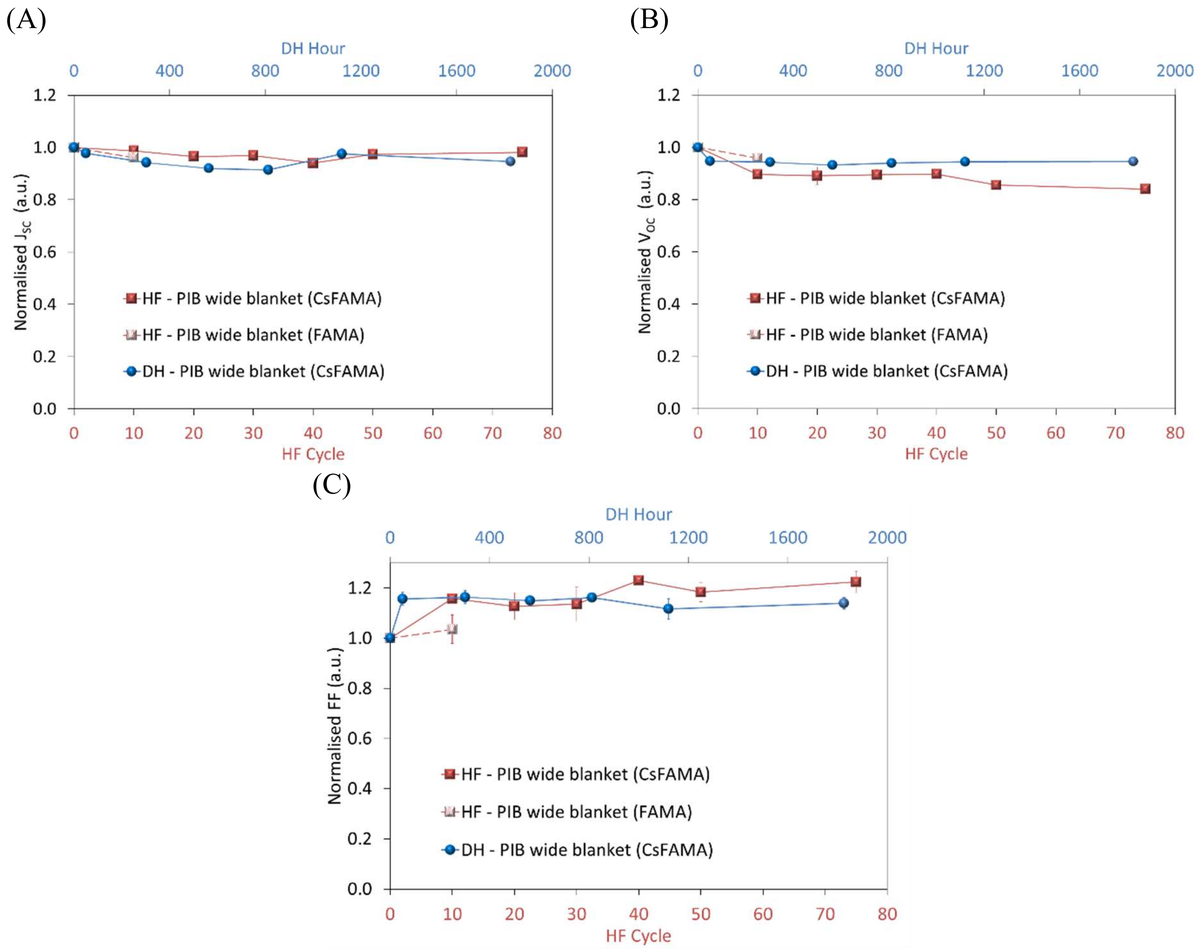

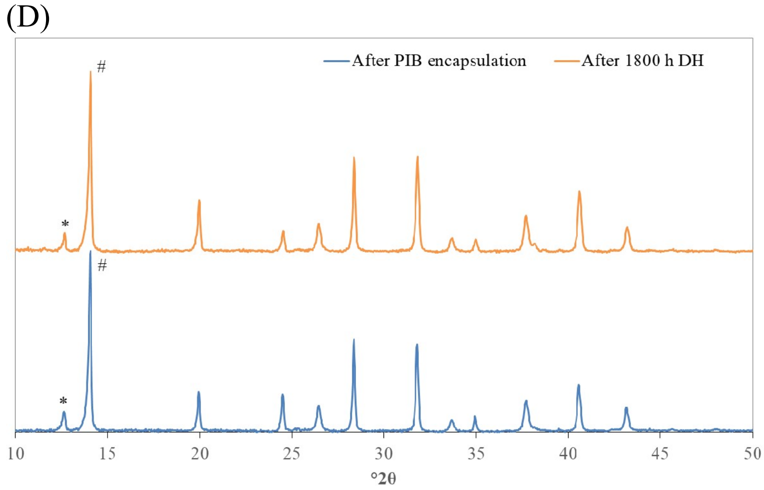

	PbI_2 (*) to Perovskite (#) peak ratio
After PIB encapsulation	0.1
After 1800 h DH	0.1

Fig. S3.

(A) J_{SC} (B) V_{OC} (C) FF evolution of PIB blanket encapsulated CsFAMA ($Cs_{0.05}FA_{0.8}MA_{0.15}Pb(I_{0.85}Br_{0.15})_3$) or FAMA ($FA_{0.85}MA_{0.15}Pb(I_{0.85}Br_{0.15})_3$) solar cells during IEC HF or DH test. D) X-ray diffraction (XRD) analysis of PIB blanket encapsulated CsFAMA PSC before and after 1800 hours of Damp Heat test. * and # denote the PbI_2 and $Cs_{0.05}FA_{0.8}MA_{0.2}(I_{0.85}, Br_{0.15})_3$ perovskite characteristic peaks, respectively. The table lists the ratios of the intensities of these two peaks.

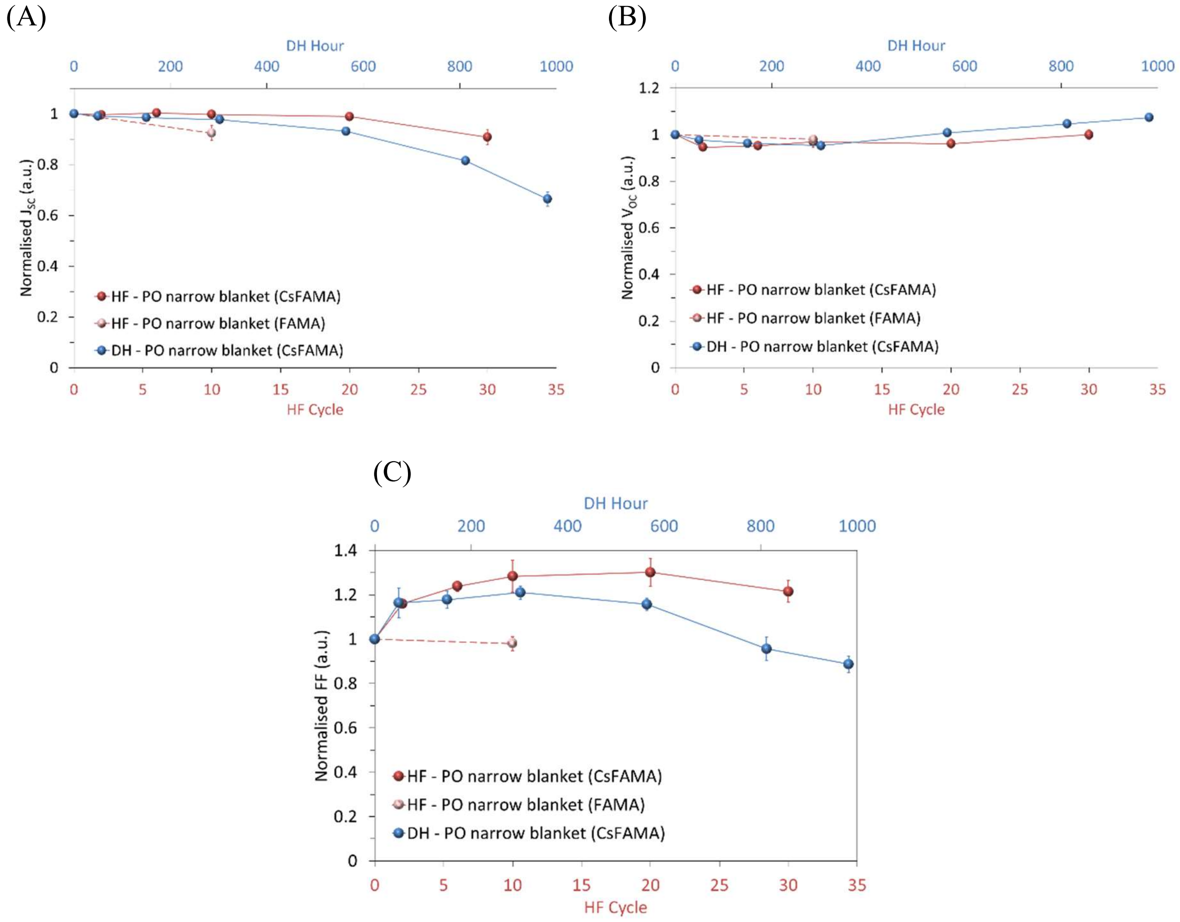

Fig. S4.

(A) J_{SC} (B) V_{OC} (C) FF evolution of PO-encapsulated CsFAMA ($Cs_{0.05}FA_{0.8}MA_{0.15}Pb(I_{0.85}Br_{0.15})_3$) or FAMA ($FA_{0.85}MA_{0.15}Pb(I_{0.85}Br_{0.15})_3$) solar cells during IEC HF and DH test.

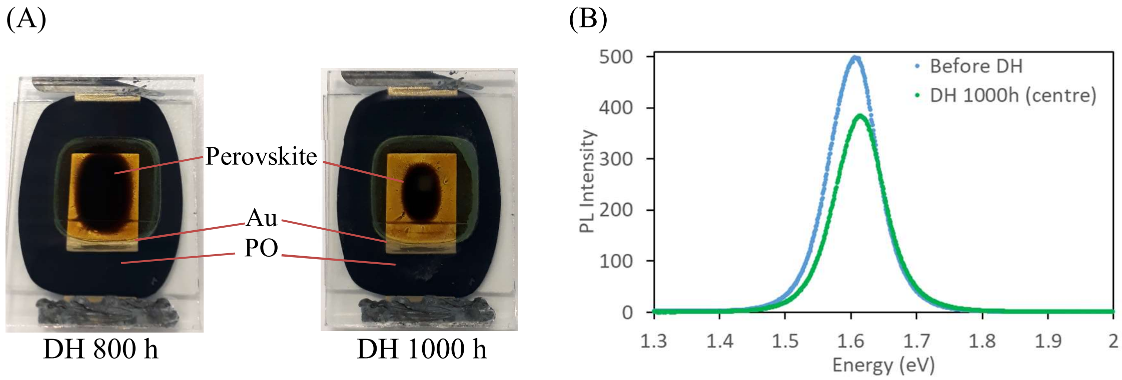

Fig. S5.

(A) Photos of a PO-encapsulated PSC after 800 h and 1000 h Damp Heat, viewed from the substrate glass side. The dark perovskite region retreated towards centre as the moisture infiltrated, revealing the underlying Au layer; (B) Spectral PL of the same PO-encapsulated PSC before DH and after 1000 h DH at "centre" black perovskite region.

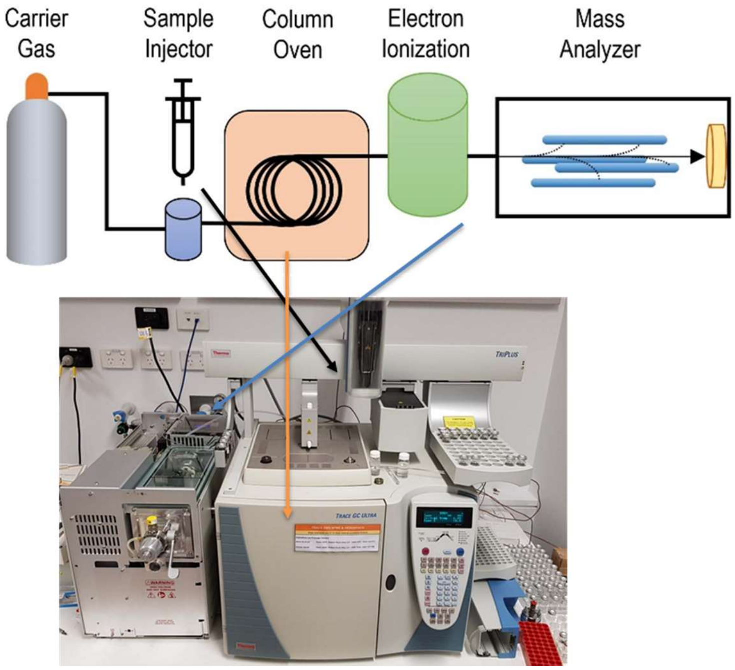

Fig. S6.

Work flow and photo of the GC-MS setup, Thermo Trace DSQ II Quadrupole GC-MS with Triplus HS autosampler (Thermo Scientific, Watham, MA)

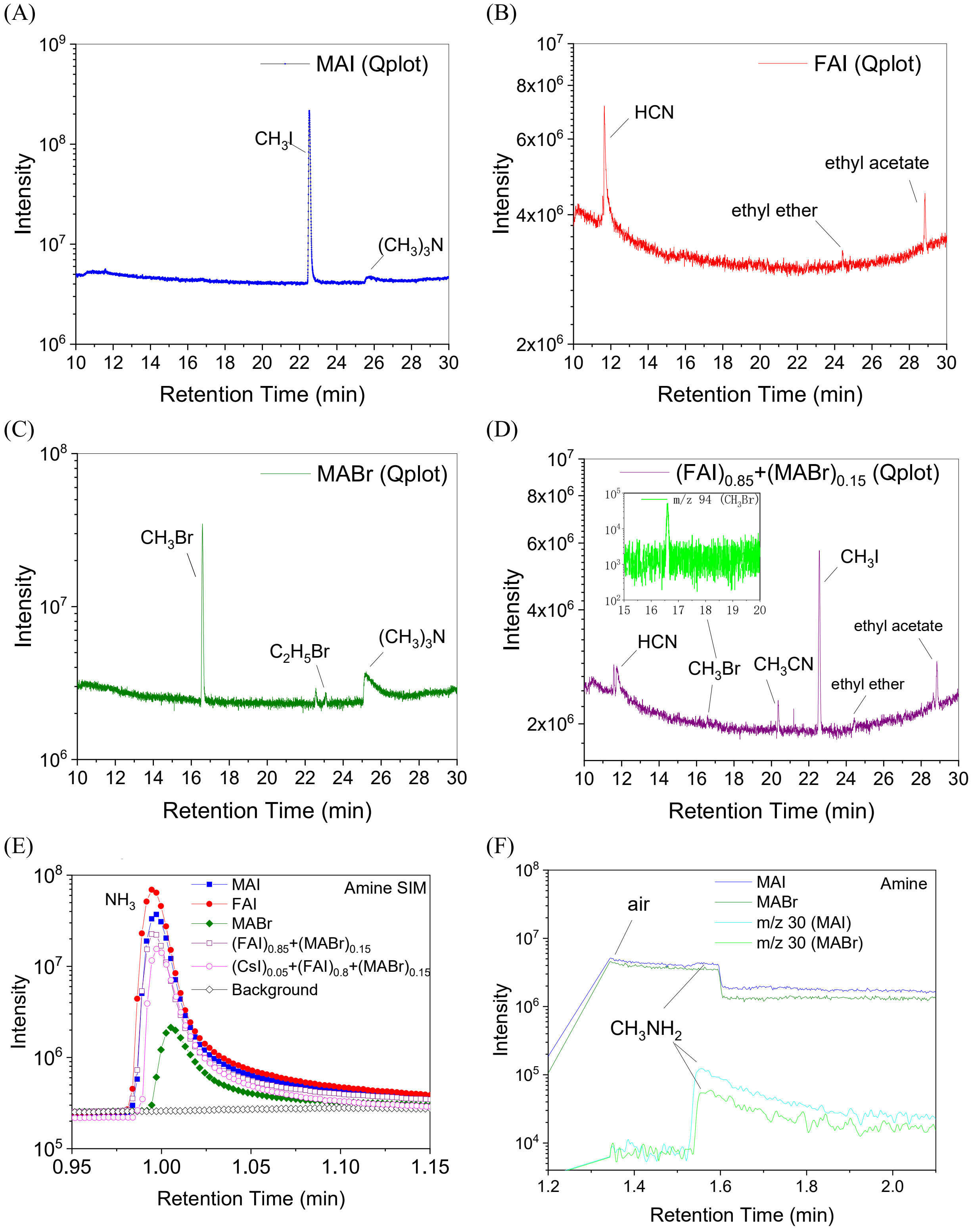
(A)
MAI (Qplot)
CH$_3$I
(CH$_3$)$_3$N
Intensity
10^6
10^7
10^8
10^9
Retention Time (min)
10 12 14 16 18 20 22 24 26 28 30
(B)
FAI (Qplot)
HCN
ethyl acetate
ethyl ether
Intensity
$2x10^6$
$4x10^6$
$6x10^6$
$8x10^6$
10^7
Retention Time (min)
10 12 14 16 18 20 22 24 26 28 30
(C)
MABr (Qplot)
CH$_3$Br
C$_2$H$_5$Br
(CH$_3$)$_3$N
Intensity
10^6
10^7
10^8
Retention Time (min)
10 12 14 16 18 20 22 24 26 28 30
(D)
(FAI)$_{0.85}$+(MABr)$_{0.15}$ (Qplot)
m/z 94 (CH$_3$Br)
10^2
10^3
10^4
10^5
15 16 17 18 19 20
HCN
CH$_3$Br
CH$_3$CN
CH$_3$I
ethyl acetate
ethyl ether
Intensity
$2x10^6$
$4x10^6$
$6x10^6$
$8x10^6$
10^7
Retention Time (min)
10 12 14 16 18 20 22 24 26 28 30
(E)
NH$_3$
MAI
FAI
MABr
(FAI)$_{0.85}$+(MABr)$_{0.15}$
(CsI)$_{0.05}$+(FAI)$_{0.8}$+(MABr)$_{0.15}$
Background
Amine SIM
Intensity
10^5
10^6
10^7
10^8
Retention Time (min)
0.95 1.00 1.05 1.10 1.15
(F)
air
CH$_3$NH$_2$
MAI
MABr
m/z 30 (MAI)
m/z 30 (MABr)
Amine
Intensity
10^4
10^5
10^6
10^7
10^8
Retention Time (min)
1.2 1.4 1.6 1.8 2.0

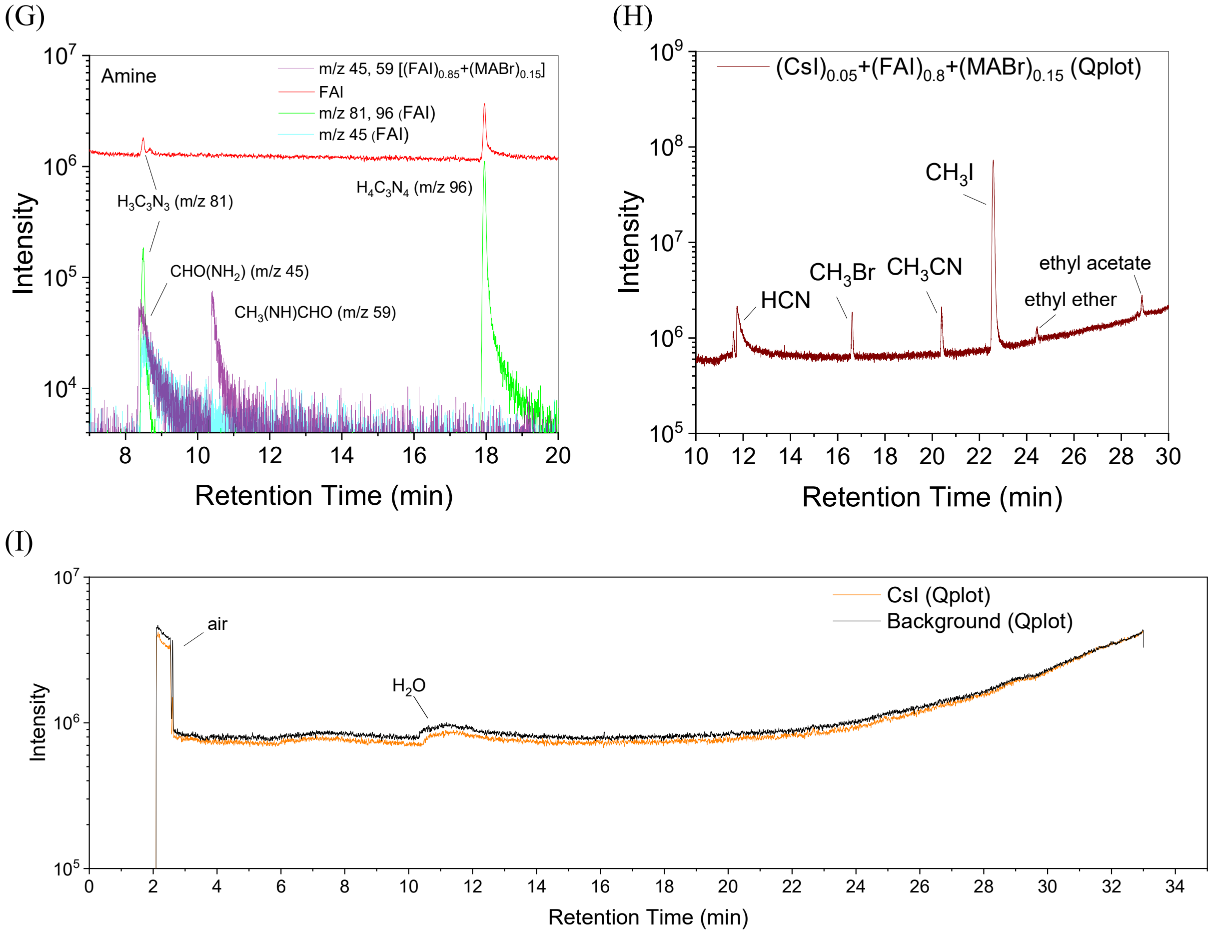

Fig. S7.

Gas chromatograms of perovskite precursor materials (A-I) after 15 minute 350 °C anneal, before loading onto the HS GC-MS system. Air, H_2O are from the background substances of the GC-MS system. Ethyl ether and ethyl acetate are likely from the original contaminants from the precursor materials. The inset in (D) is the plot of m/z 94 which corresponds to the characteristic mass spectrum of CH_3Br.

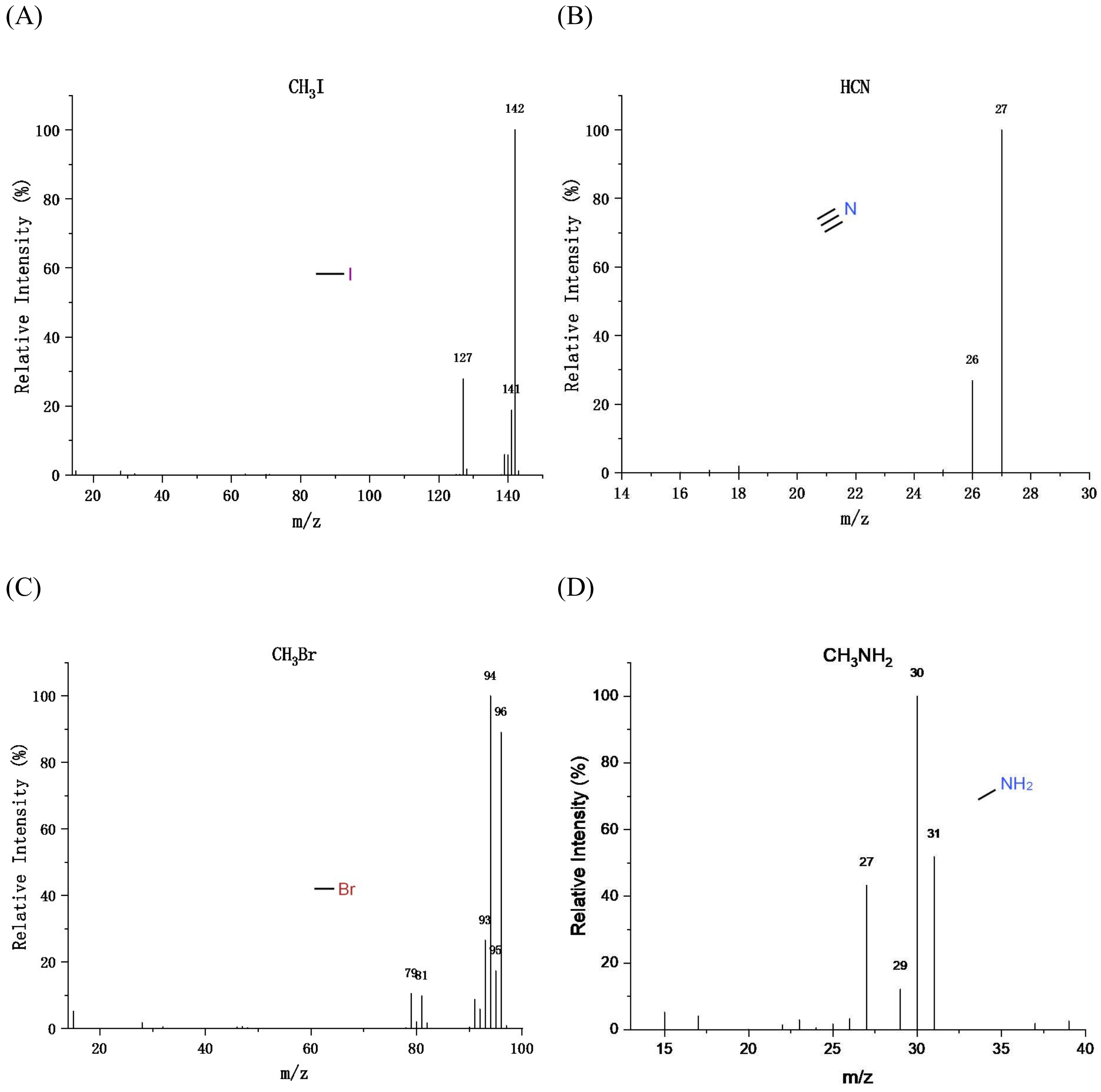
(A)
CH$_3$I
Relative Intensity (%)
m/z
0
20
40
60
80
100
20
40
60
80
100
120
140
142
127
141
I
(B)
HCN
Relative Intensity (%)
m/z
0
20
40
60
80
100
14
16
18
20
22
24
26
28
30
27
26
N
(C)
CH$_3$Br
Relative Intensity (%)
m/z
0
20
40
60
80
100
20
40
60
80
100
94
96
93
95
79
81
Br
(D)
CH$_3$NH$_2$
Relative Intensity (%)
m/z
0
20
40
60
80
100
15
20
25
30
35
40
30
31
27
29
NH$_2$

(E)

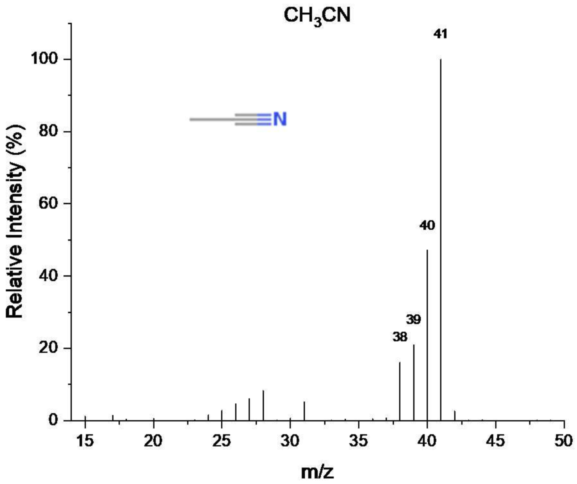
CH$_3$CN
N
Relative Intensity (%)
0
20
40
60
80
100
m/z
15
20
25
30
35
40
45
50
38
39
40
41

(F)

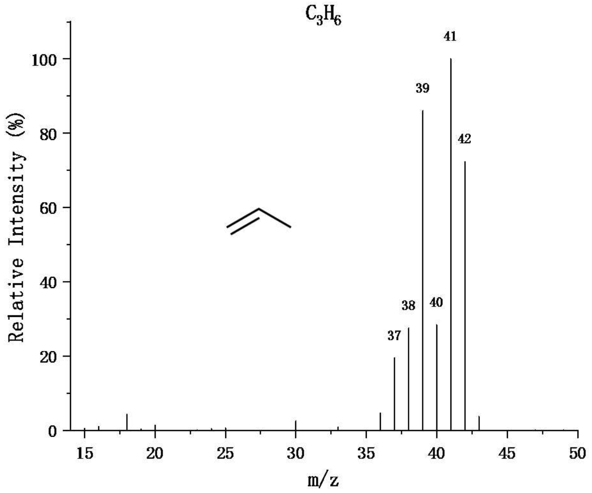
C$_3$H$_6$
Relative Intensity (%)
0
20
40
60
80
100
m/z
15
20
25
30
35
40
45
50
37
38
39
40
41
42

(G)

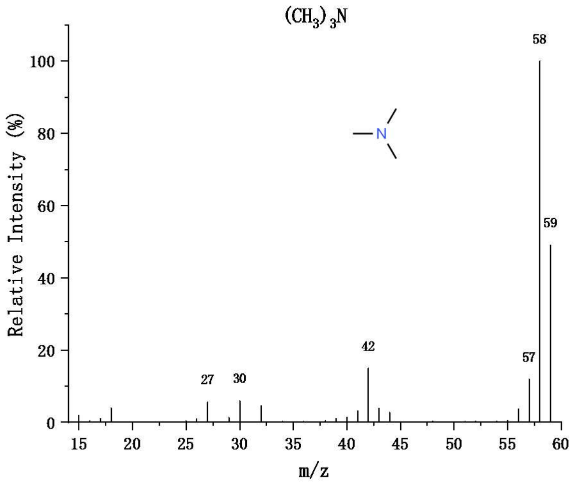
(CH$_3$)$_3$N
N
Relative Intensity (%)
0
20
40
60
80
100
m/z
15
20
25
30
35
40
45
50
55
60
27
30
42
57
58
59

(H)

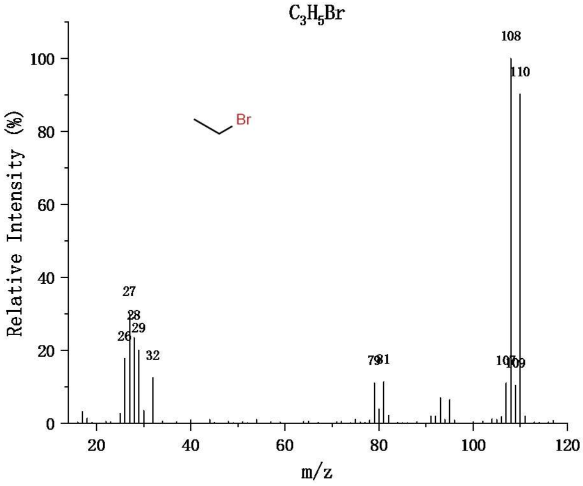
C$_3$H$_5$Br
Br
Relative Intensity (%)
0
20
40
60
80
100
m/z
20
40
60
80
100
120
26
27
28
29
32
79
81
107
108
109
110

(I)

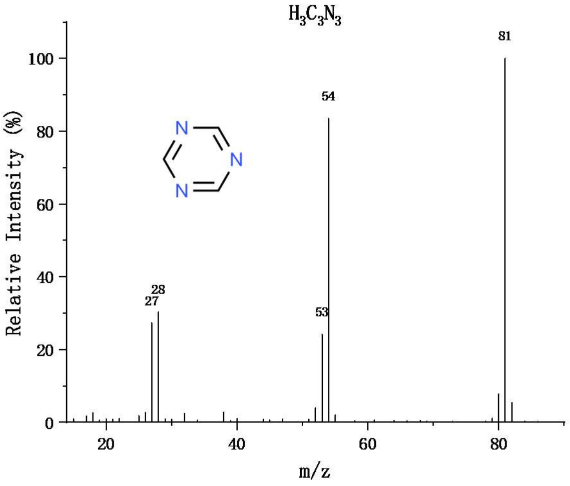
$H_3C_3N_3$
Relative Intensity (%)
0
20
40
60
80
100
m/z
20
40
60
80
27
28
53
54
81
N
N
N

(J)

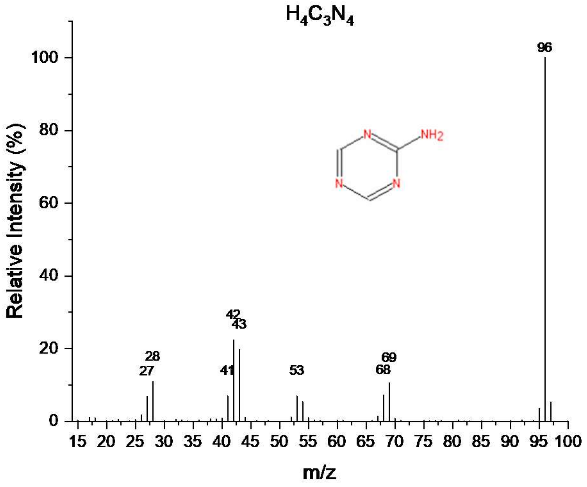
$H_4C_3N_4$
Relative Intensity (%)
0
20
40
60
80
100
m/z
15 20 25 30 35 40 45 50 55 60 65 70 75 80 85 90 95 100
27
28
41
42
43
53
68
69
96
N
N
N
NH2

(K)

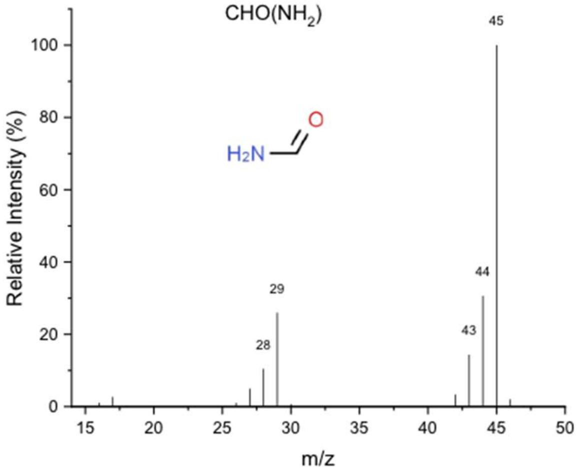
CHO(NH$_2$)
Relative Intensity (%)
0
20
40
60
80
100
m/z
15 20 25 30 35 40 45 50
28
29
43
44
45
H2N
O

(L)

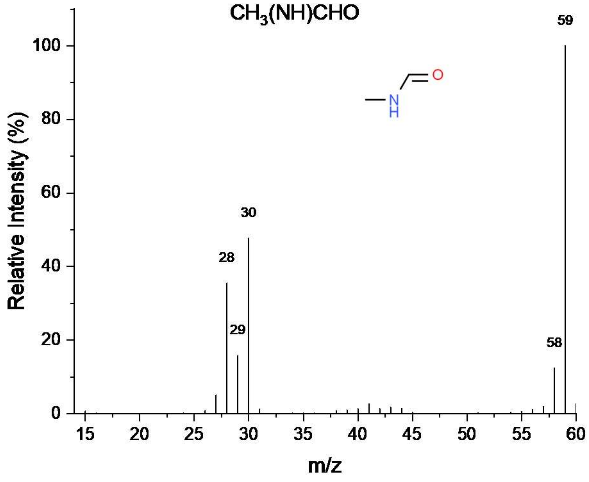
CH$_3$(NH)CHO
Relative Intensity (%)
0
20
40
60
80
100
m/z
15 20 25 30 35 40 45 50 55 60
28
29
30
58
59
N
H
O

(M)

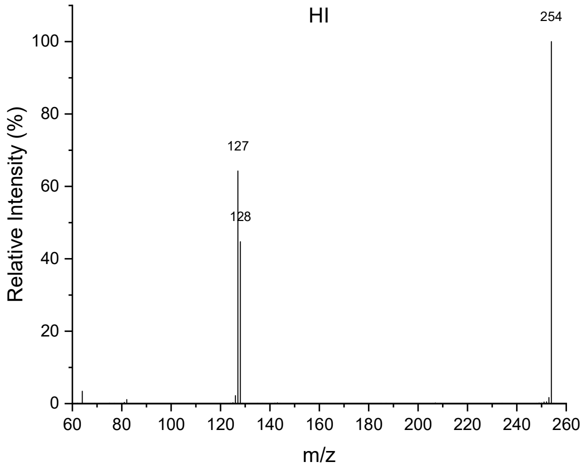

Fig. S8.

Measured mass spectra of the gas chromatograms related to perovskite precursor material decompositions

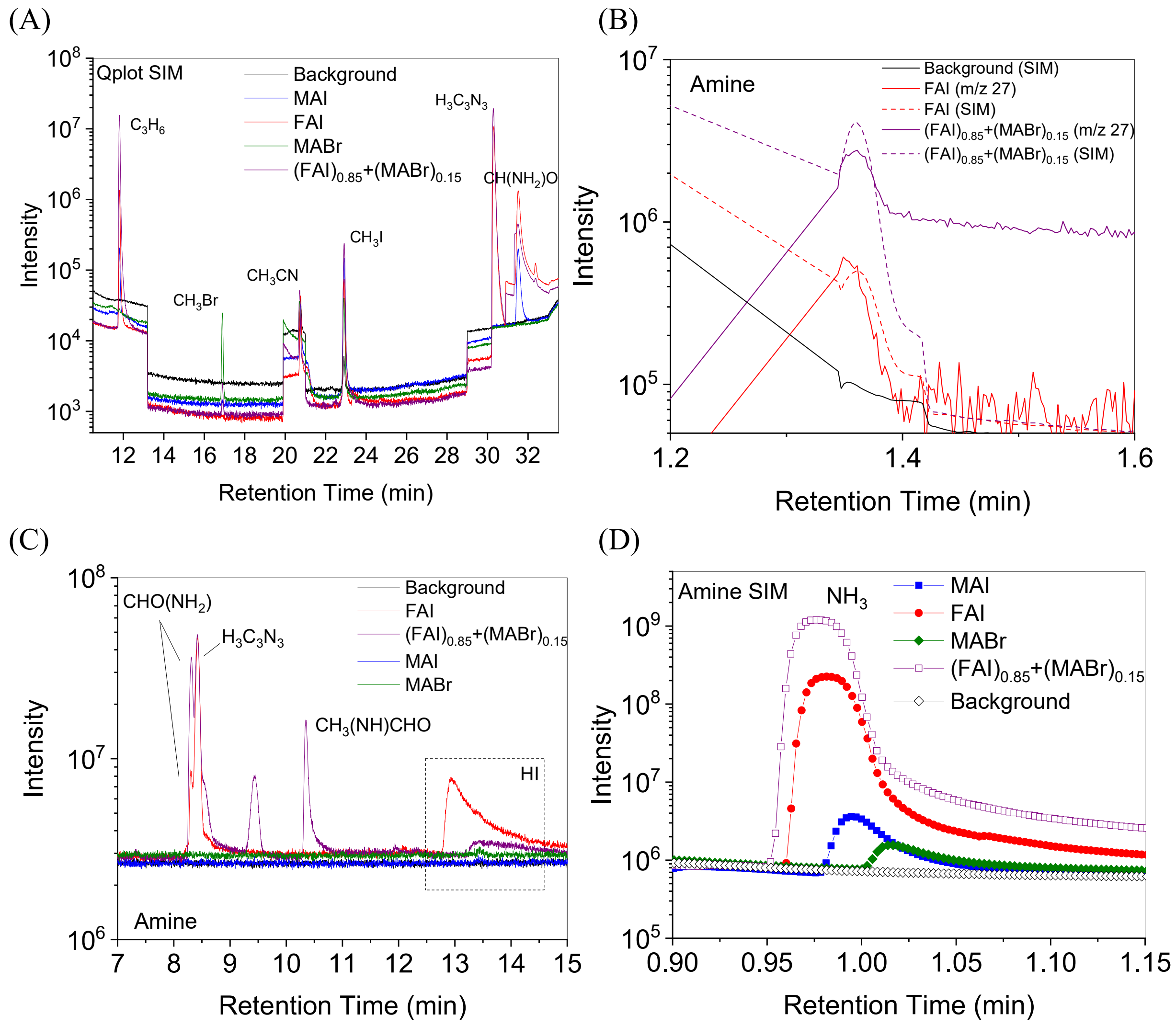

Fig. S9.

Gas chromatograms (before GC-MS measurement) of perovskite precursor materials after 10 hour 140 °C anneal for (A) all perovskite powders (Qplot method (SIM)), (B) FAI and $(FAI)_{0.85}$ + $(MABr)_{0.15}$ powders (Amine method) showing the HCN (m/z 27) peaks only, (C) all perovskite powders (Amine method) showing $H_3C_3N_3$ (*sym*-triazine), $CHO(NH_2)$ (formamide), $CH_3(NH)CHO$ (methylformide) and HI peaks , and (D) all perovskite powders (Amine method) showing NH_3 only . Note the different retention times for HI detected from different perovskite powders, indicating the poor reproducibility of HI detection by VolatileAmine column for the reason explained in Direct MS analysis method section.

(A)

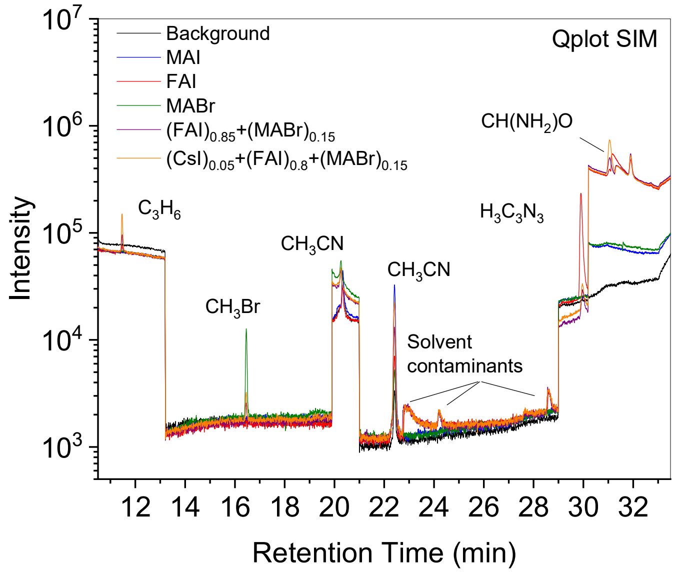
Qplot SIM
Background
MAI
FAI
MABr
$(FAI)_{0.85}+(MABr)_{0.15}$
$(CsI)_{0.05}+(FAI)_{0.8}+(MABr)_{0.15}$
C_3H_6
CH_3Br
CH_3CN
CH_3CN
Solvent contaminants
$H_3C_3N_3$
$CH(NH_2)O$
Intensity
10^7
10^6
10^5
10^4
10^3
12
14
16
18
20
22
24
26
28
30
32
Retention Time (min)

(B)

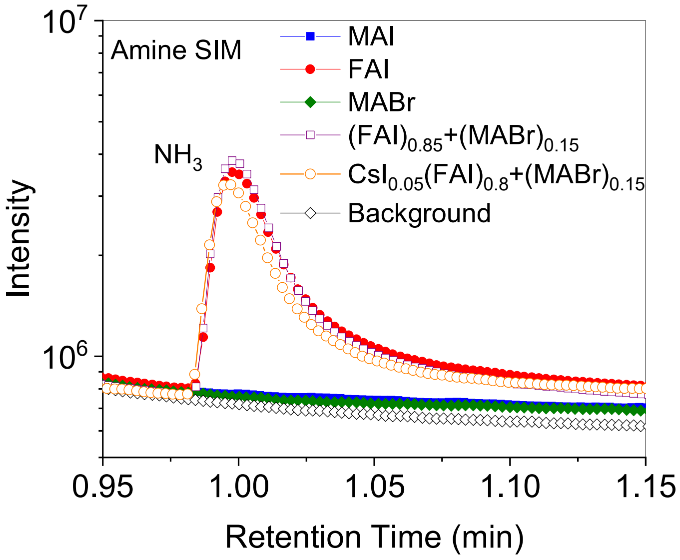
Amine SIM
MAI
FAI
MABr
$(FAI)_{0.85}+(MABr)_{0.15}$
$CsI_{0.05}(FAI)_{0.8}+(MABr)_{0.15}$
Background
NH_3
Intensity
10^7
10^6
0.95
1.00
1.05
1.10
1.15
Retention Time (min)

(C)

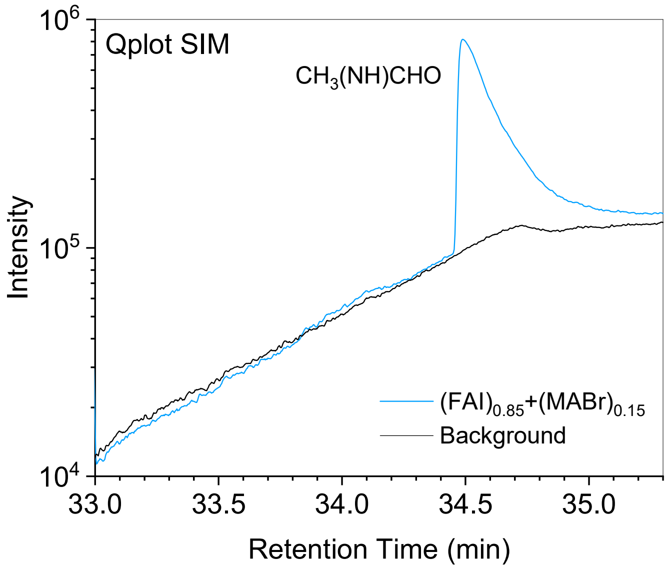

Fig. S10.

Gas chromatograms before the GC-MS measurement of perovskite powders after 100 hour 85 °C anneal obtained by (A) Qplot SIM method (B) Amine SIM method for NH_3 only and (C) of $FAI_{0.85}$ + $MABr_{0.15}$ powder highlighting the $CH_3(NH)CHO$ peak by Qplot SIM method

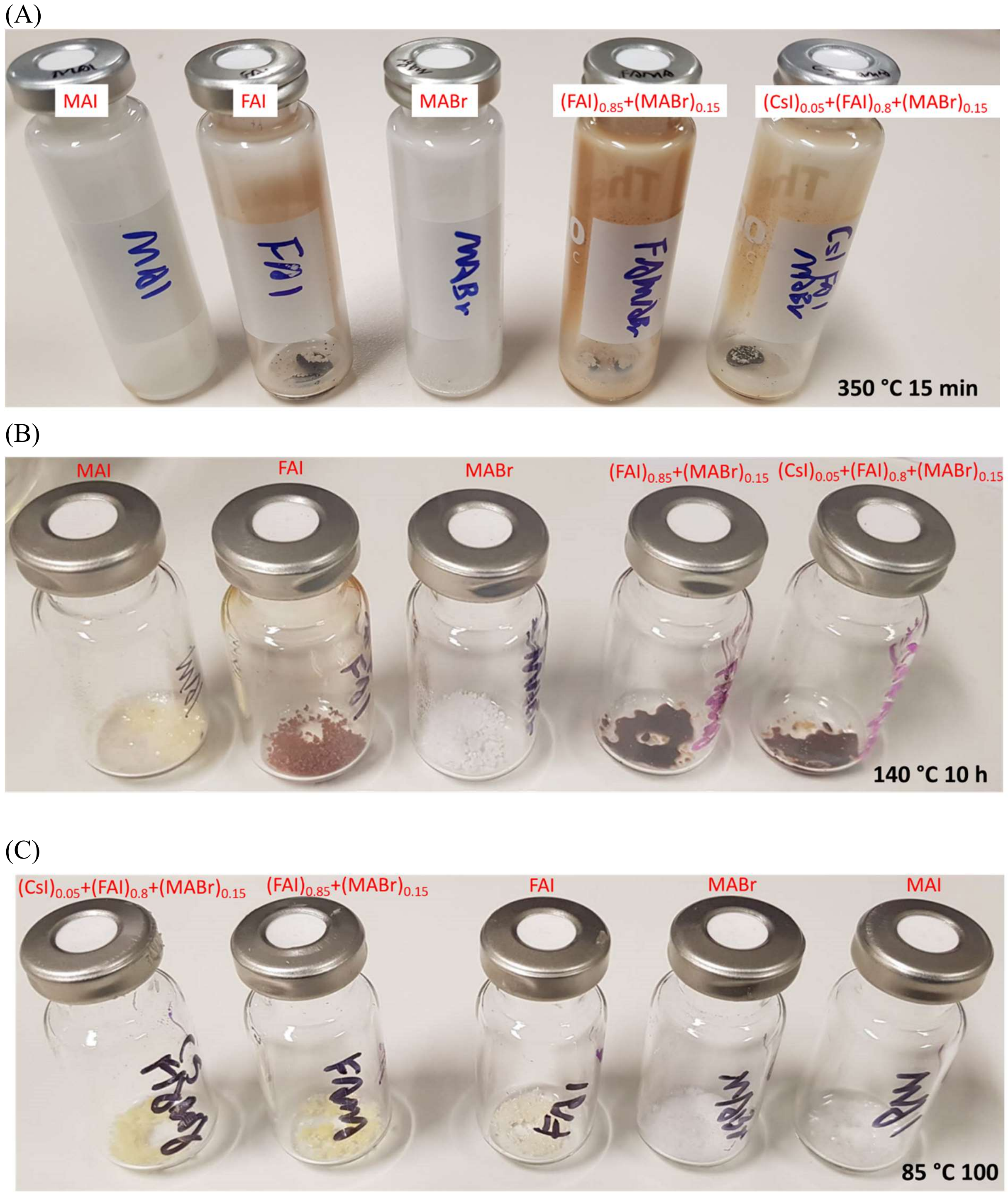

Fig. S11.

Photos of perovskite precursor powders which were sealed in N_2 in glass vials and annealed at (A) 350°C for 15 minutes; (B) 140 °C for 10 hours and (B) 85 °C for 100 hours.

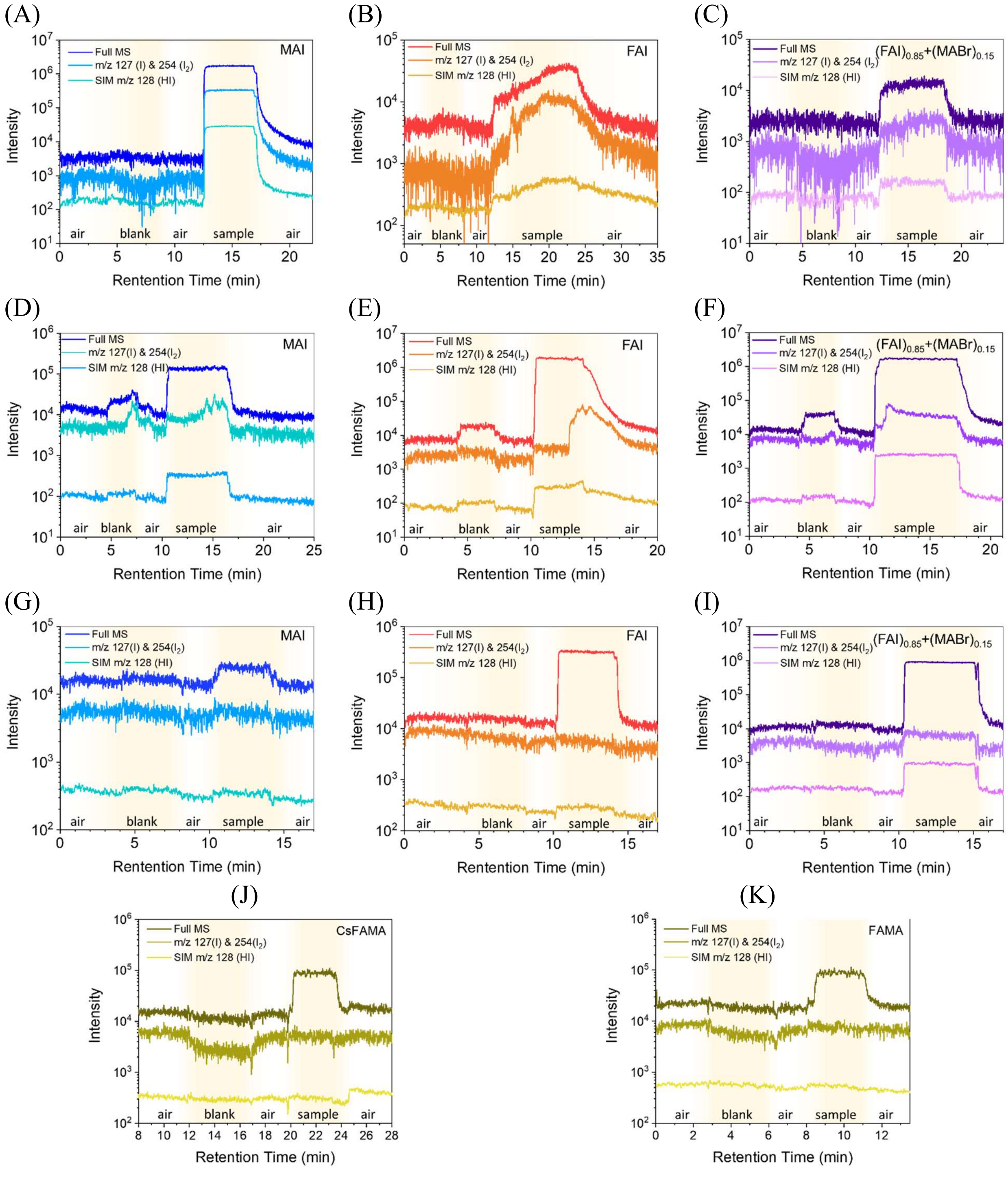

Fig. S12.

Direct Introduction MS for HI measurement for iodine containing perovskite precursors annealed at (A-C) 350 °C for 15 minutes, (D-F) 140 °C for 10 hours and (G-I) at 85 °C for 100 hours. Direct Introduction MS for HI measurement for for un-encapsulated (J) CsFAMA or (K) FAMA test cells annealed at 85 °C for 100 hours. Similar to Fig. S4E, the regions of "air", "blank" and "sample" correspond to different gas extraction stages of Direct MS method.

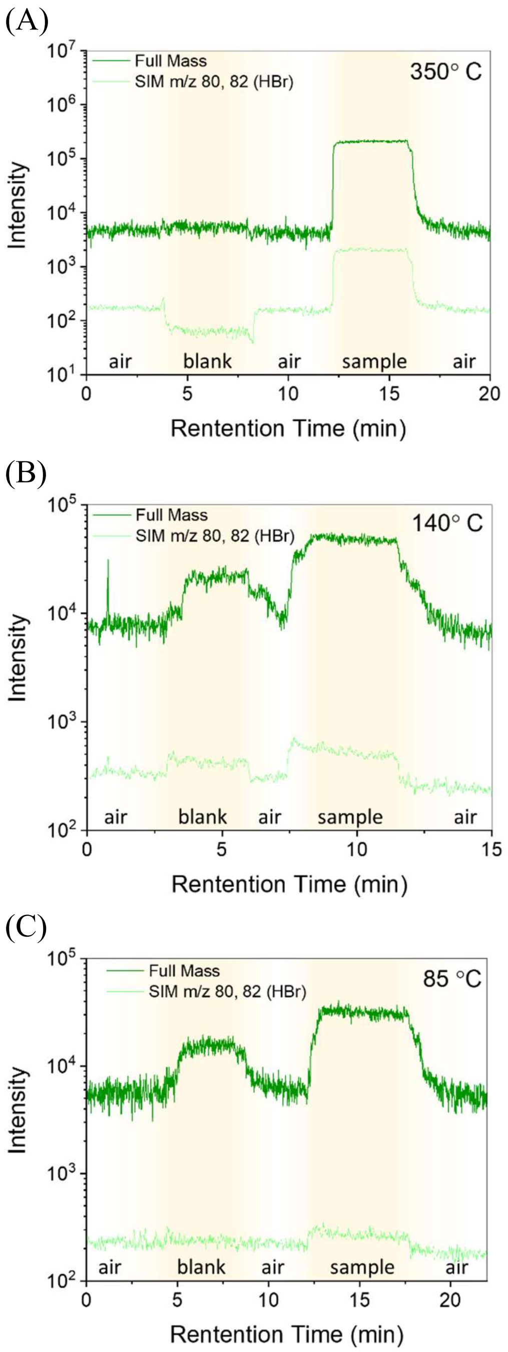

Fig. S13.

Direct Introduction MS for HBr measurement from MABr powders annealed at (A) 350 °C for 15 min, (b) 140 °C for 10 h and (C) 85 °C for 100 h. Similar to Fig. S4E, the regions of "air", "blank" and "sample" correspond to different gas extraction stages of Direct MS analysis.

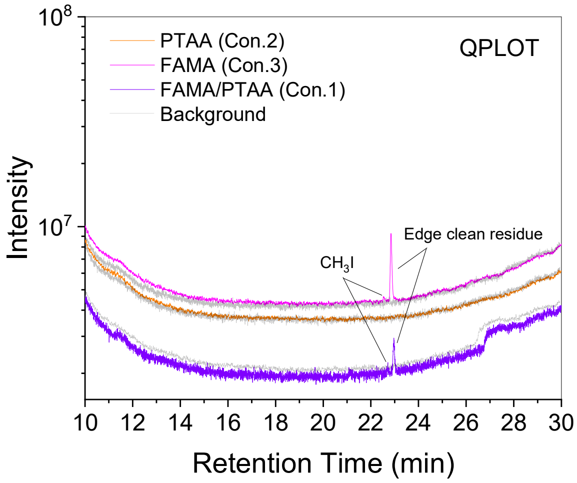

Fig. S14.

GC chromatograms for FAMA (Con.1), PTAA (Con.2) and FAMA/PTAA (Con.3) by QPlot Method. The highest peaks are the chemical residue resulting from the edge treatment. No edge treatment was done for PTAA samples (Con.2). The figure also shows the peaks for CH_3I which are hardly noticeable under the full scan mode of QPlot Method.

(A)

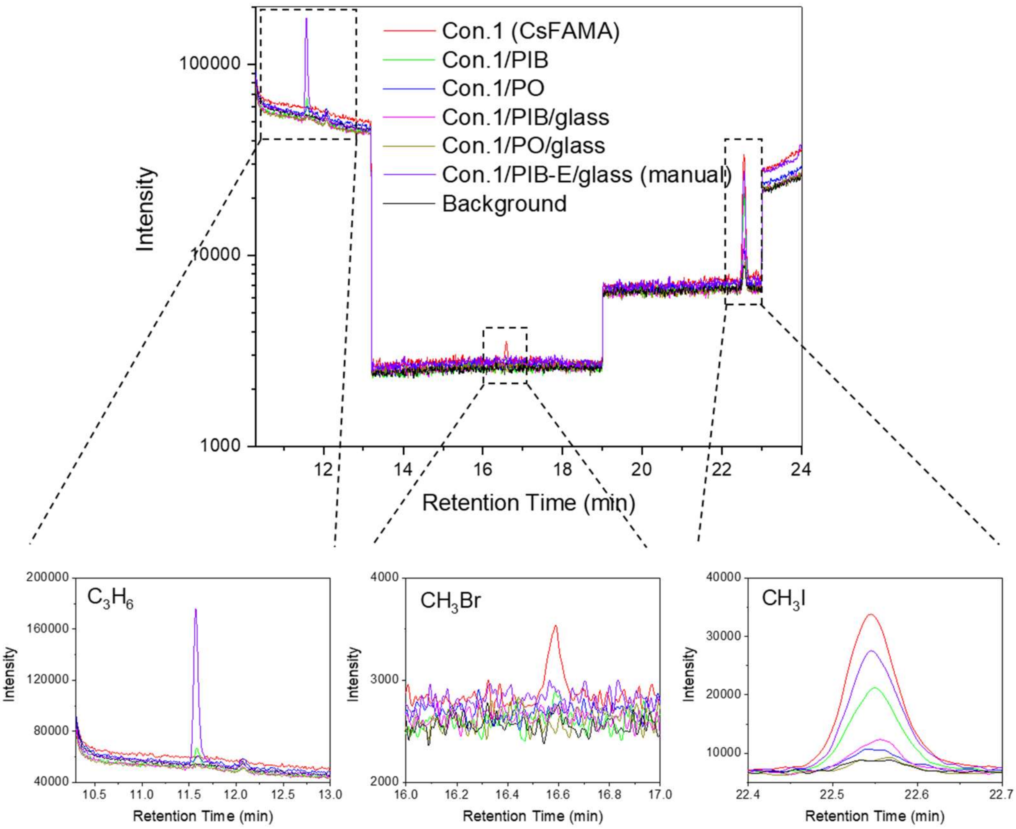
Con.1 (CsFAMA)
Con.1/PIB
Con.1/PO
Con.1/PIB/glass
Con.1/PO/glass
Con.1/PIB-E/glass (manual)
Background
Intensity
100000
10000
1000
12
14
16
18
20
22
24
Retention Time (min)
C_3H_6
200000
160000
120000
80000
40000
10.5
11.0
11.5
12.0
12.5
13.0
CH_3Br
4000
3000
2000
16.0
16.2
16.4
16.6
16.8
17.0
CH_3I
40000
30000
20000
10000
22.4
22.5
22.6
22.7

(B)

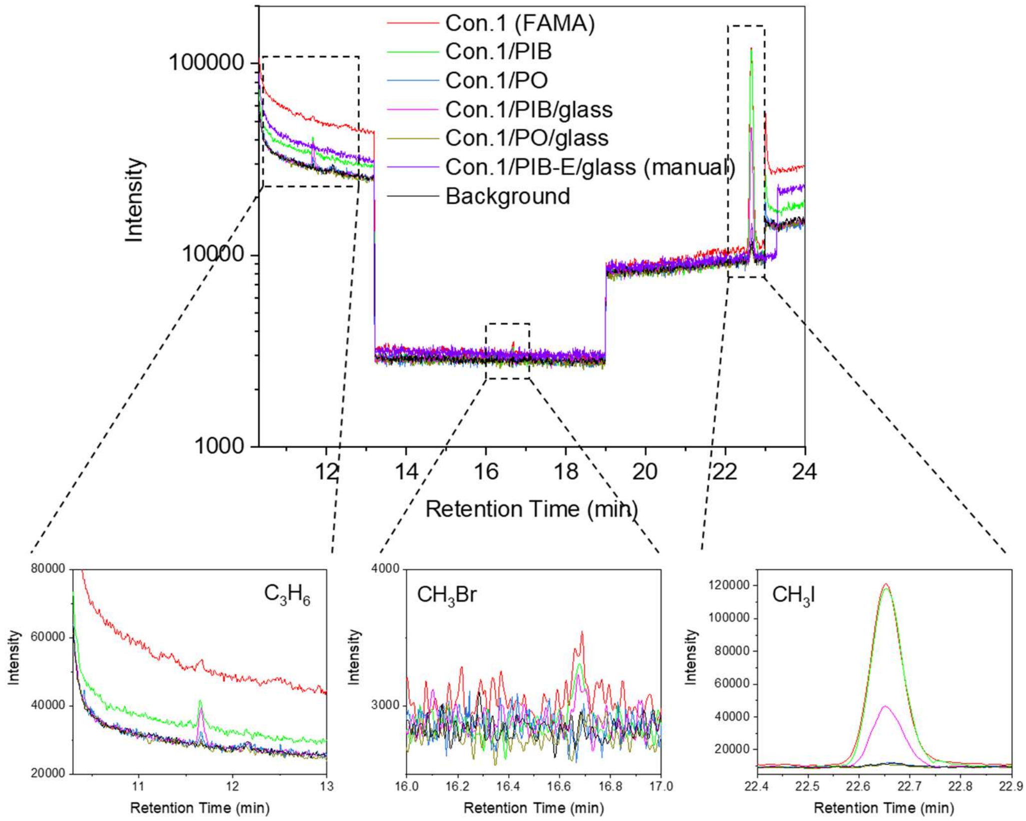

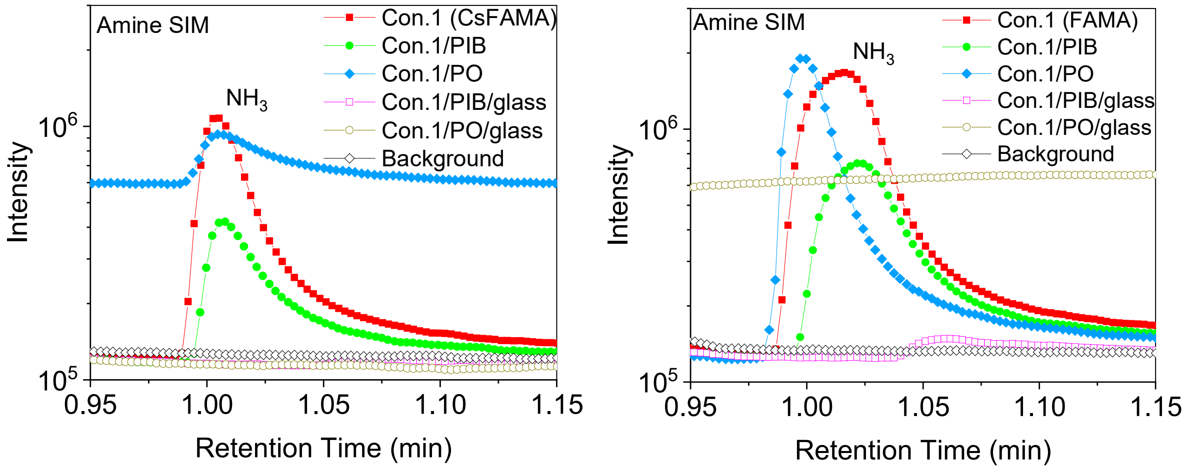
(C) CsFAMA

(D) FAMA

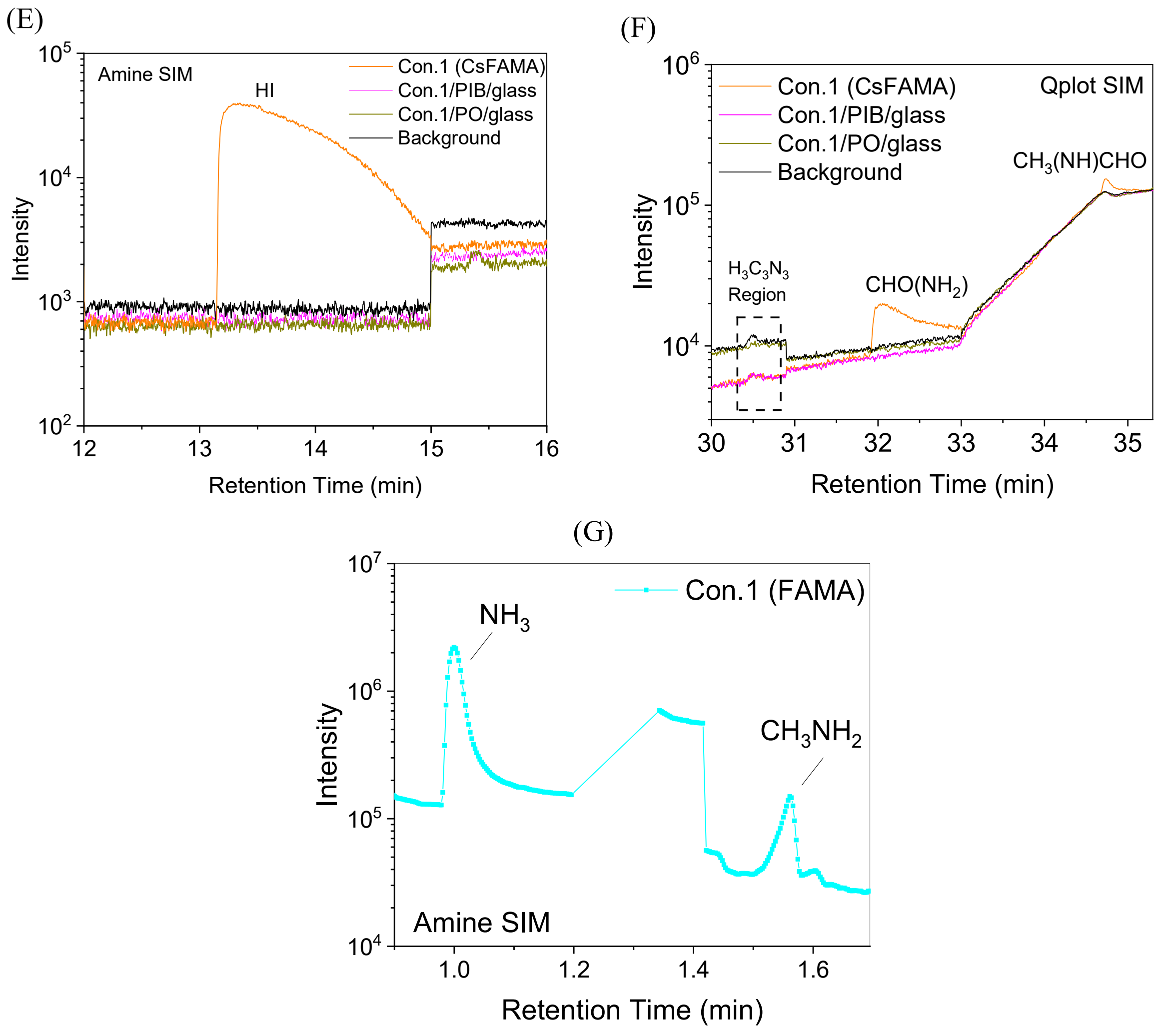

Fig. S15.

Gas chromatograms for C_3H_6 (from the outgassing of PIB and PO based polymers); CH_3Br; CH_3I of un-encapsulated and encapsulated (A) CsFAMA and (B) FAMA PSC's detected by QPLOT method. Gas chromatograms for NH_3 of un-encapsulated and encapsulated (C) CsFAMA and (D) FAMA PSC's detected by Amine method. Gas chromatogram for HI of un-encapsulated and encapsulated (E) CsFAMA PSC's detected by Amine method. (F) Gas chromatograms for un-encapsulated and encapsulated CsFAMA for $CHO(NH_2)$ (formamide) and $CH_3(NH)CHO$ (methyformamide). Note the absence (below background) of $H_3C_3N_3$. (G) Gas chromatogram for NH_3 and CH_3NH_2 of un-encapsulated FAMA PSC detected by Amine method. Note for encapsulated cells, HI, $CHO(NH_2)$ and $CH_3(NH)CHO$ are greatly diminished. The analytes were quantified using SIM methods.

(A)

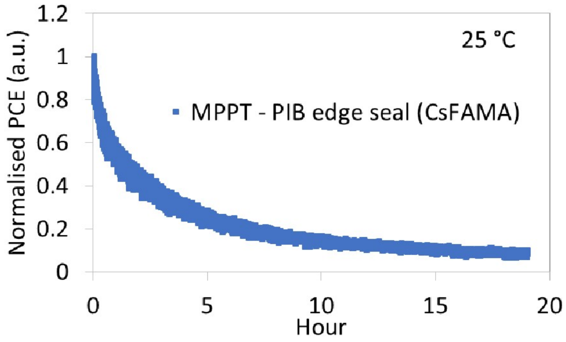
Normalised PCE (a.u.)
1.2
1
0.8
0.6
0.4
0.2
0
25 °C
MPPT - PIB edge seal (CsFAMA)
0
5
10
15
20
Hour

(B)

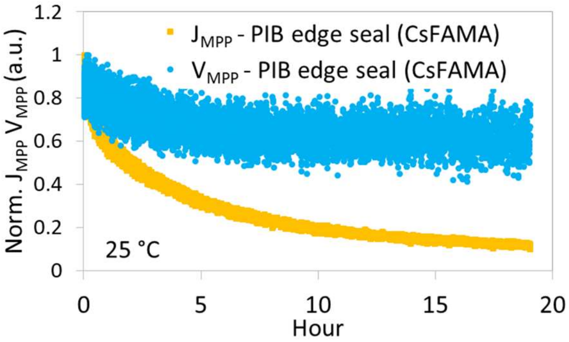
Norm. J_{MPP} V_{MPP} (a.u.)
1.2
1
0.8
0.6
0.4
0.2
0
J_MPP - PIB edge seal (CsFAMA)
V_MPP - PIB edge seal (CsFAMA)
25 °C
0
5
10
15
20
Hour

(C)

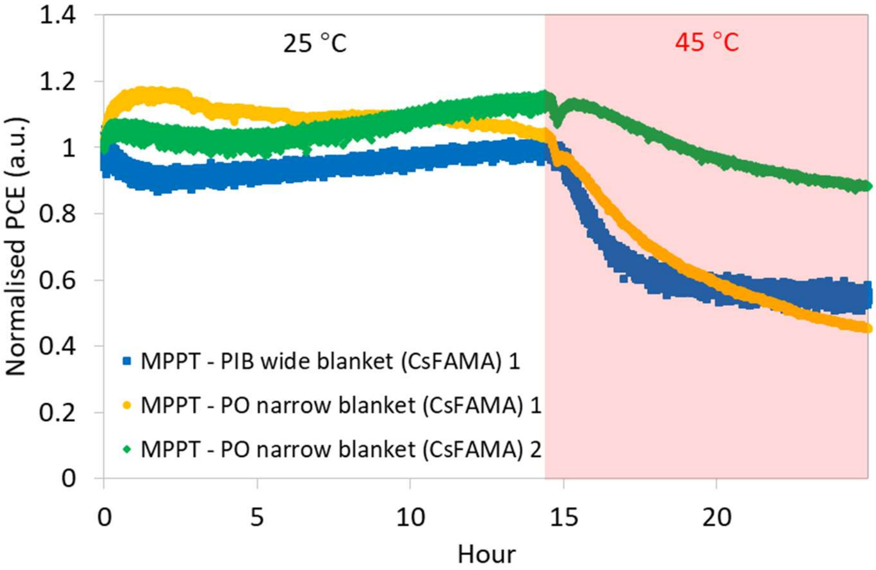
Normalised PCE (a.u.)
1.4
1.2
1
0.8
0.6
0.4
0.2
0
25 °C
45 °C
MPPT - PIB wide blanket (CsFAMA) 1
MPPT - PO narrow blanket (CsFAMA) 1
MPPT - PO narrow blanket (CsFAMA) 2
0
5
10
15
20
Hour

(D)

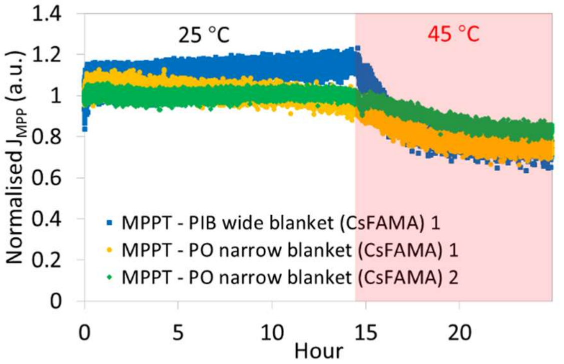
Normalised J_MPP (a.u.)
1.4
1.2
1
0.8
0.6
0.4
0.2
0
25 °C
45 °C
MPPT - PIB wide blanket (CsFAMA) 1
MPPT - PO narrow blanket (CsFAMA) 1
MPPT - PO narrow blanket (CsFAMA) 2
0
5
10
15
20
Hour

(E)

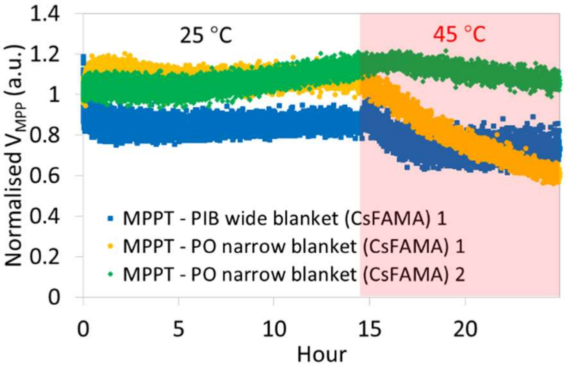
Normalised V_MPP (a.u.)
1.4
1.2
1
0.8
0.6
0.4
0.2
0
25 °C
45 °C
MPPT - PIB wide blanket (CsFAMA) 1
MPPT - PO narrow blanket (CsFAMA) 1
MPPT - PO narrow blanket (CsFAMA) 2
0
5
10
15
20
Hour

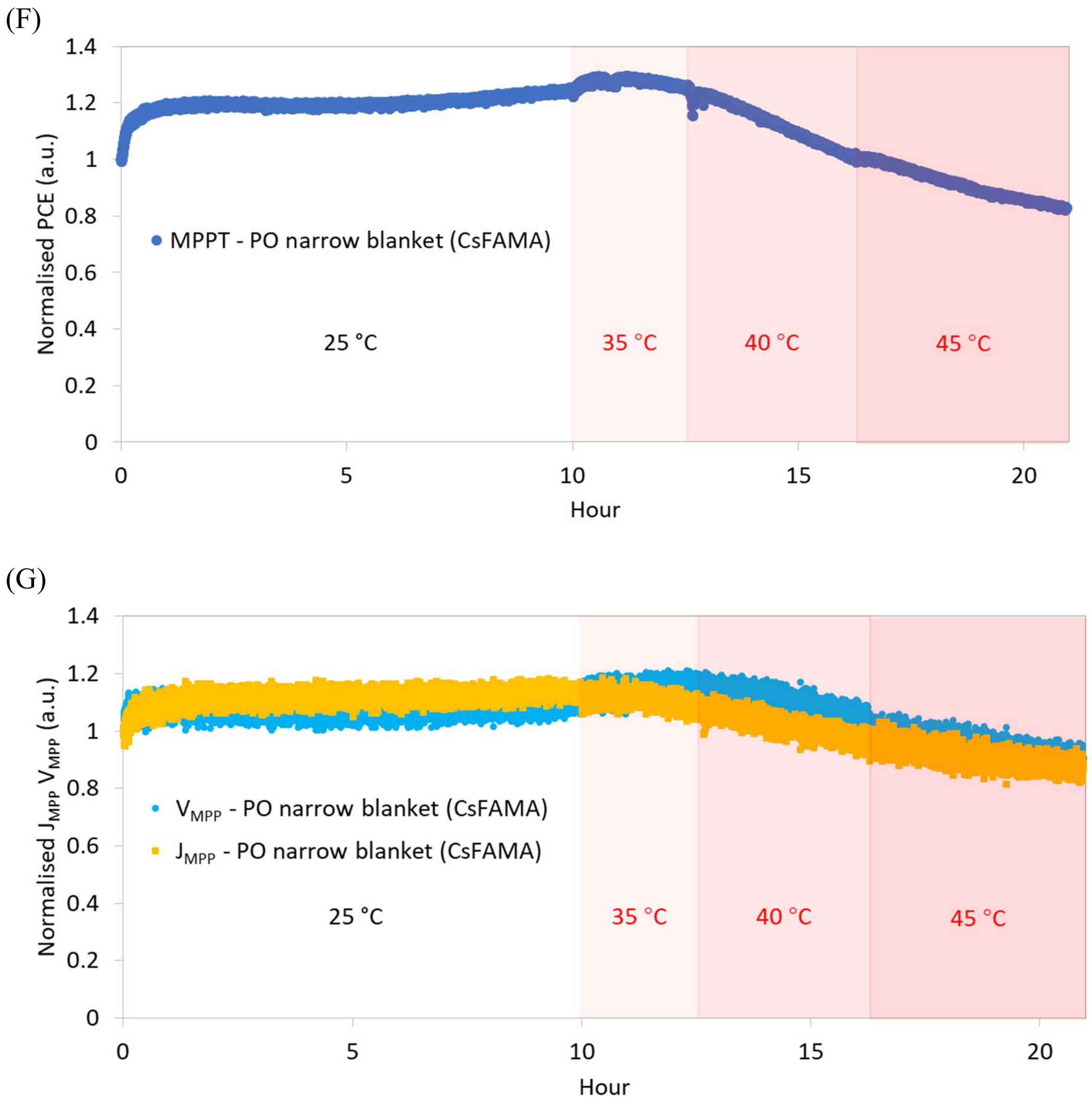

Fig. S16.

Maximum power point (MPP) tracking (MPPT) CsFAMA cells under AM1.5G 1 sun with temperature variation. (A) Normalised PCE and (B) corresponding J_{MPP} and V_{MPP} of PIB edge sealed cells. (C) Normalised PCE and corresponding (D) J_{MPP} and (D) V_{MPP} of one wide PIB blanket encapsulated and two narrow PO blanket encapsulated cells at 25°C and 45°C. (F) Normalised PCE and corresponding (G) J_{MPP} and V_{MPP} of one narrow PO blanket encapsulated cell at 25°C, 35°C, 40°C and 45°C.

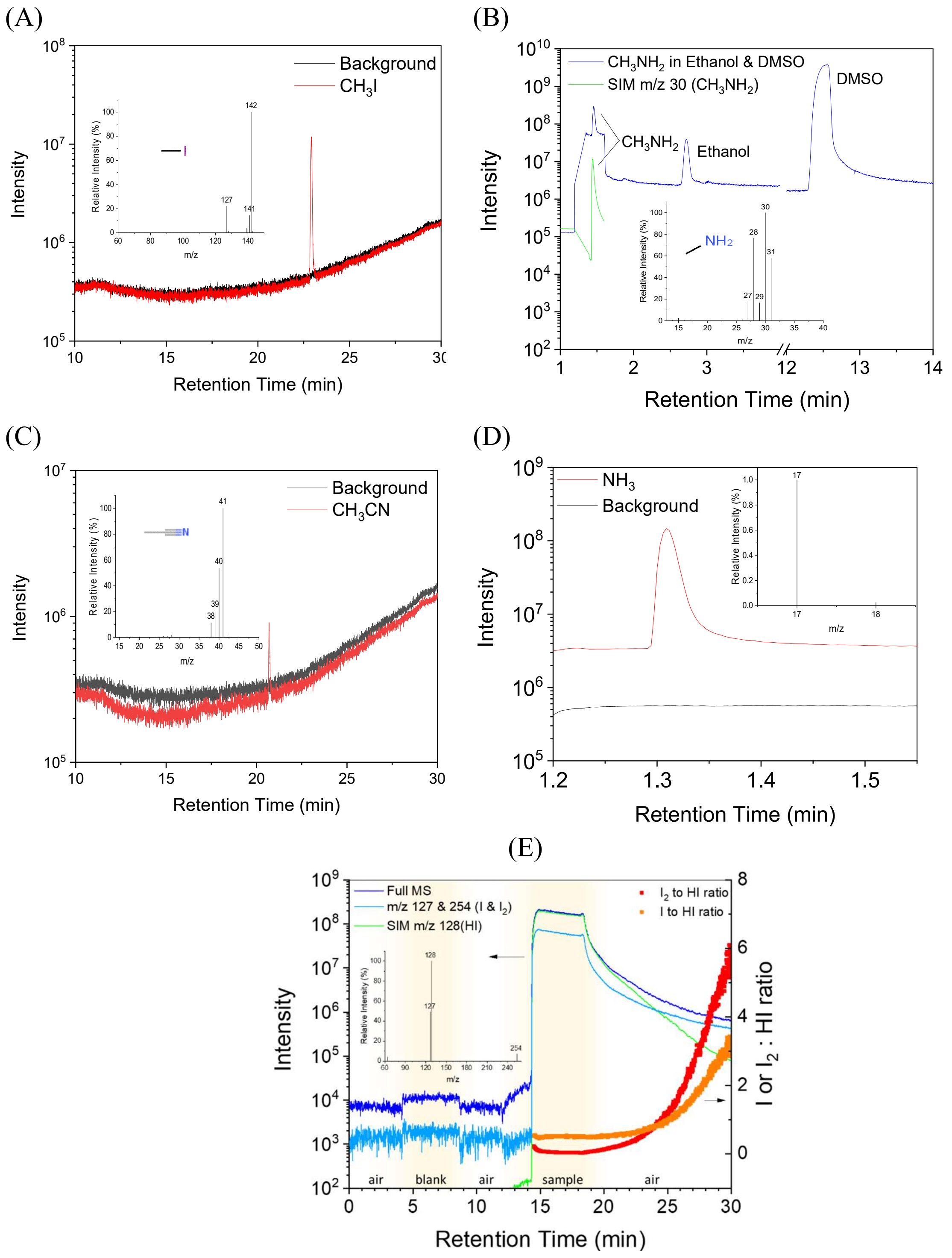

Fig. S17.

Gas chromatograms of standard gas samples of (A) CH_3I; (B) CH_3NH_2; (C) CH_3CN; and (D) NH_3. Direct MS analysis for (E) HI. The ratio of iodine (I) to HI and the ratio of iodine gas (I_2) to HI are also plotted. The regions labelled “air”, “blank” and “sample” correspond to different gas extraction stages of Direct MS analysis. The measured mass spectrum of the standard gas is shown as the inset in each figure.

Table S1. Thermally stable PSC's at 85 °C testing condition.

Structure	Initial PCE	Stability Test	Barrier	Encapsulation	Lifetime (T_{95}/T_{80})*	Ref.
ITO/NiO/CsFAPbIBr/LiF/PCBM/SnO_2/ITO-ZTO/ITO/Ag	10.1 %[#]	85 °C / 85 %RH	SnO_2/ITO-ZTO/ITO/	glass / EVA-butyl rubber / glass	>1000 h	(*46*)
ITO/NiO_X/$MAPbI_3$/PCBM/SnO_2/ITO/Ag	10.1 - 13.1 %	85 °C in N_2	SnO_2/ITO	no	>1000 h	(*49*)
ITO/NiO/$Cs_{0.17}FA_{0.83}Pb(I_{0.83}Br_{0.17})_3$/LiF/$C_{60}$/$SnO_2$/ITO-ZTO/ITO/Ag	11.1 - 12.8 %[#]	85 °C / 85 %RH	SnO_2/ITO-ZTO/ITO	PO-butyl rubber / glass	>1000 h	(*52*)
FTO/TiO_2/Al_2O_3/NiO/$Cs_{0.05}(FA_{0.4}MA_{0.6})_{0.95}PbI_{2.8}Br_{0.2}$/C	17.0 %	85 °C / 40-60 %RH	C	no	>1000 h	(*75*)
ITO/NiO_X/$MAPbI_3$/$PC_{61}BM$/AZO/Ag	15.2 %	85 °C / 5 %RH	AZO	Epoxy / glass	>1000 h	(*76*)
FTO/c-TiO_2/$FAPbI_3$/PTAA/Au	8.3-9.2%	85 °C / 85 %RH	no	PIB / glass	>500 h	(*25*)
FTO/c-TiO_2/mp-TiO_2/RbCsFAMAPbIBr/PTAA/Au	17.3 %	85 °C in N_2 / AM1.5 MPPT	no	no	>500 h	(*34*)
FTO/NiMgLiO/$MAPbI_3$/graphene-PCBM/CQDs/Ag	15.6 %	85 °C / 50 %RH	graphene-PCBM/CQDs	epoxy / glass	>500 h	(*43*)
FTO/c-TiO_2/mp-TiO_2/$FAPbI_3$/CuPc/Au	17.5 %[^]	85 °C in N_2	no	no	>400 h / >1100 h	(*40*)
FTO/NiO/$Cs_{0.05}MA_{0.95}PbI_3$/PCBM/BCP/AZO/Ag	18.5 %	85 °C / 20-60 %RH, MPPT (UV filter)	AZO	no	>200 h / >500 h	(*47*)
FTO/c-TiO_2/$(Cs_{0.2}FA_{0.8})Pb(I_{0.95}Br_{0.05})_3$/PTAA/CuPc/Au	16.0 %	85 °C	no	no	~150 h / >550 h	(*77*)
ITO/SnO_2/$FAMAPbI_3$/PEAI/PTAA/Au	23.3 %	85 °C in N_2	no	no	<10 h / >500 h	(*78*)

* T_{95}/T_{80} = time when the efficiency drops to 95 % / 80 % of the initial value.
# top cell in a tandem device
^ Highest reported PCE.
ZTO = zinc tin oxide
FTO = fluorine doped tin oxide
PCBM = phenyl-C61-butyric acid methyl ester
CQD = colloidal quantum dot
CuPc = copper(II) phthalocyanine

BCP = bathocuproine
PEAI = phenethylammonium iodide
PTAA = poly[bis(4-phenyl)(2,4,6-trimethylphenyl)amine]

Table S2. Properties and material costs of the polymers used in this work in comparison to EVA and epoxy^

	PO	**PVS 101**	**EVA+**	**UV-cured epoxy**
WVTR (g/m^2/day) +23 °C, 100 %RH.	$<10^{-3}$	10^{-2} – 10^{-3}	28	16
Application temperature (°C)	140 – 170	RT – 160	140 – 150	RT
Calculated* cost as an edge sealant (US$)	0.34	0.22	N/A	145
Calculated* cost as an encapsulant (US$)	10.6	6.8	4.4	N/A

RT = room temperature
*price calculations are based on a module with a length of 1190 mm and a width of 789.5 mm.
+EVA used in this work has a price of US$2/m^2. A single layer of EVA is typically used to encapsulate a thin-film solar panel.
^The prices and the application guides for PO, PIB and UV-cured epoxy were obtained from suppliers.

Table S3. Vacuum lamination parameters for the two sealants.

	Temperature	Step 1	Step 2
PIB based polymer	95 °C	0.5 mbar, 5 min	500 mbar, 5 min
PO based polymer	140 °C	0.5 mbar, 2 min	800 mbar, 6 min

Table S4. PCE measured before and after encapsulation using PIB (PVS 101) or PO based polymer.

	PIB		PO	
PCE (%)	Before	After	Before	After
Reverse scan	14.1	13.8	11.8	11.9
Forward scan	13.0	12.9	8.2	8.6
Average	13.5	13.3	10.0	10.3

Table S5. PCE of an edge sealed PSC measured under reverse scan, forward scan and at stabilised maximum power point, before and after 200 h Damp Heat test.

PCE (%)	Reverse scan	Forward scan	Average	Stabilised
Before DH	11.8	11.1	11.4	11.4
DH 200 h	9.4	9.1	9.2	9.2

Table S6A. Qplot method parameters (Restek Rt-QPLOT column)

Procedure/sample	Perovskite powders 350 °C	Perovskite powders & cells 140 °C	Perovskite powders 85 °C	Perovskite thin films & cells & PTAA thin films 85 °C
Incubation temp. (°C)	95	145	90	95
Incubation time (min)	15	15	15	15
Syringe temp. (°C)	130	150	95	150
Gas volume injected (mL)	0.4	0.4	0.4	0.4
PTV inlet temp. (°C)	200	150	150	200
Split ratio	100:1	5:1	5:1	5:1
Carrier Gas flow rate (mL/min)	2	2	2	2
Gas saver flow rate (mL/min)	30	-	-	-
Gas saver start time (min)	4	-	-	-
Transfer line temp. (°C)	250	250	250	250
Ion source temp. (°C)	200	200	200	200
Solvent delay (min)	2.1	2.1	2.1	2.1
MS scan range (m/z)	14-400	14-260 or SIM (Table S6B)	14-260 or SIM (Table S6B)	14-200 or SIM (Table S6B)
MS scan rate (scans/sec)	7	3.9 or SIM	3.9 or SIM	5 or SIM
Oven temp. profile	The GC oven has an initial temperature of 40 ° C for 6 min, which increases at a rate of 10 °C/min to 90 °C, then a rate of 5 °C/min to 200 °C, and then 30 °C/min to a final temperature of 250 °C, where it is hold for 2 minutes.			

Table S6B. Qplot method MS – SIM parameters

Seg#	Start (min)	Ion (*m/z*)	Dwell (ms)	Width (*m/z*)
1	10.30	27.1, 41.1	80	0.1
2	13.20	94	180	0.1
3	19.90	41.1	180	0.1
4	21.5	142	180	0.2
5	29	81.06	180	0.1
6	30.9	45.07	180	0.1
7	33	59.1	180	0.1

Table S7A. Amine method parameters (Restek Rtx-VolatileAmine column)

Procedure/sample	Perovskite powders 350 °C	Perovskite powders 350 °C (NH_3 only)	Perovskite powders 140 °C	Perovskite powders, thin films, cells & PTAA thin films 85 °C	Perovskite thin films, cells & PTAA thin films 85 °C (NH_3 only)
Incubation temp. (°C)	95	70	145	90	70
Incubation time (min)	15	10	15	15	10
Syringe temp. (°C)	100	80	150	110	80
Gas volume injected (mL)	0.4	0.3	0.4	0.4	0.3
PTV inlet temp. (°C)	120	120	150	150	120
Carrier Gas flow rate (mL/min)	3.3	3.3	3.3	3.3	3.3
Split ratio	50:1	100:1	5:1	5:1	3:1
Gas saver flow rate (mL/min)	50	30	50	50	-
Gas saver start time (min)	5	1.5	5	5	-
Transfer line temp. (°C)	155	155	155	155	155
Ion source temp. (°C)	190	180	190	190	180
Solvent delay (min)	0.8	0.8	0.8	0.8	0.8
MS scan range (m/z)	Table S7B	Table S7C	Table S7B&D	Table S7B&D	Table S7C
MS scan rate (scans/sec)	7 or SIM	6.3 or SIM	7 or SMI	7 or SIM	6.3 or SIM
Oven temp. profile	The GC oven has an initial temperature of 30 °C for 1 min, which increases at a rate of 20 °C/min to 150 °C and is hold for 2 minutes.				

Table S7B. Amine method parameters MS parameters (350 °C, 140 °C and 85 °C)

Seg#	Start (min)	Ion (*m/z*)	Dwell (ms)	Width (*m/z*)
1	0.8	17.2	140	0.1
2	1.2	off	-	-
3	1.3	12-260	-	-

Table S7C. Amine method parameters MS – SIM parameters (NH_3 only)

Seg#	Start (min)	Ion (*m/z*)	Dwell (ms)	Width (*m/z*)
1	0.8	17.2	140	0.1
2	1.2	off	n/a	n/a

Table S7D. Amine method parameters MS – SIM parameters (140 °C and 85 °C)

Seg#	Start (min)	Ion (*m/z*)	Dwell (ms)	Width (*m/z*)
1	0.8	17.2	140	0.1
2	1.2	off	-	-
3	1.3	27.03	140	0.1
4	1.42	30.05	140	0.1
5	2.33	93.9	140	0.1
6	2.8	41.05	140	0.1
7	3.5	141.9	140	0.1
8	5.3	off	-	-
9	8.0	45.03, 81, 152.9	80	0.1
10	10.0	59.1	100	0.1
11	12.0	253.9	100	0.1
12	15.0	69	100	0.1

References

1. M. A. Green, A. Ho-Baillie, H. J. Snaith, The emergence of perovskite solar cells. *Nat. Photonics* **8**, 506–514 (2014). doi:10.1038/nphoton.2014.134

2. M. A. Green, A. Ho-Baillie, Perovskite Solar Cells: The Birth of a New Era in Photovoltaics. *ACS Energy Lett.* **2**, 822–830 (2017). doi:10.1021/acsenergylett.7b00137

3. M. A. Green, E. D. Dunlop, J. Hohl-Ebinger, M. Yoshita, N. Kopidakis, A. W. Y. Ho-Baillie, Solar cell efficiency tables (version 54). *Prog. Photovolt. Res. Appl.* **28**, 3–15 (2020). doi:10.1002/pip.3228

4. National Renewable Energy Laboratory, Efficiency Chart (2019); https://www.nrel.gov/pv/cell-efficiency.html.

5. N. L. Chang, A. W. Yi Ho-Baillie, P. A. Basore, T. L. Young, R. Evans, R. J. Egan, A manufacturing cost estimation method with uncertainty analysis and its application to perovskite on glass photovoltaic modules. *Prog. Photovolt. Res. Appl.* **25**, 390–405 (2017). doi:10.1002/pip.2871

6. J. H. Noh, S. H. Im, J. H. Heo, T. N. Mandal, S. I. Seok, Chemical management for colorful, efficient, and stable inorganic-organic hybrid nanostructured solar cells. *Nano Lett.* **13**, 1764–1769 (2013). doi:10.1021/nl400349b Medline

7. S. N. Habisreutinger, T. Leijtens, G. E. Eperon, S. D. Stranks, R. J. Nicholas, H. J. Snaith, Carbon nanotube/polymer composites as a highly stable hole collection layer in perovskite solar cells. *Nano Lett.* **14**, 5561–5568 (2014). doi:10.1021/nl501982b Medline

8. G. Niu, W. Li, F. Meng, L. Wang, H. Dong, Y. Qiu, Study on the stability of $CH_3NH_3PbI_3$ films and the effect of post-modification by aluminum oxide in all-solid-state hybrid solar cells. *J. Mater. Chem. A* **2**, 705–710 (2014). doi:10.1039/C3TA13606J

9. J. A. Christians, P. A. Miranda Herrera, P. V. Kamat, Transformation of the excited state and photovoltaic efficiency of $CH_3NH_3PbI_3$ perovskite upon controlled exposure to humidified air. *J. Am. Chem. Soc.* **137**, 1530–1538 (2015). doi:10.1021/ja511132a Medline

10. M. I. Asghar, J. Zhang, H. Wang, P. D. Lund, Device stability of perovskite solar cells – A review. *Renew. Sustain. Energy Rev.* **77**, 131–146 (2017). doi:10.1016/j.rser.2017.04.003

11. J. Huang, S. Tan, P. Lund, H. Zhou, Impact of H_2O on organic-inorganic hybrid perovskite solar cells. *Energy Environ. Sci.* **10**, 2284–2311 (2017). doi:10.1039/C7EE01674C

12. P. Wang, Y. Wu, B. Cai, Q. Ma, X. Zheng, W. Zhang, Solution-Processable Perovskite Solar Cells toward Commercialization—Progress and Challenges. *Adv. Funct. Mater.* **29**, 1807661 (2019). doi:10.1002/adfm.201807661

13. A. Dualeh, N. Tétreault, T. Moehl, P. Gao, M. K. Nazeeruddin, M. Grätzel, Effect of annealing temperature on film morphology of organic-inorganic hybrid pervoskite solid-state solar cells. *Adv. Funct. Mater.* **24**, 3250–3258 (2014). doi:10.1002/adfm.201304022

14. B. Conings, J. Drijkoningen, N. Gauquelin, A. Babayigit, J. D'Haen, L. D'Olieslaeger, A. Ethirajan, J. Verbeeck, J. Manca, E. Mosconi, F. De Angelis, H. G. Boyen, Intrinsic Thermal Instability of Methylammonium Lead Trihalide Perovskite. *Adv. Energy Mater.* **5**, 1500477 (2015). doi:10.1002/aenm.201500477

15. B. Philippe, B.-W. Park, R. Lindblad, J. Oscarsson, S. Ahmadi, E. M. J. Johansson, H. Rensmo, Chemical and Electronic Structure Characterization of Lead Halide Perovskites and Stability Behavior under Different Exposures - a Photoelectron Spectroscopy Investigation. *Chem. Mater.* **27**, 1720–1731 (2015). doi:10.1021/acs.chemmater.5b00348

16. N. K. Kim, Y. H. Min, S. Noh, E. Cho, G. Jeong, M. Joo, S. W. Ahn, J. S. Lee, S. Kim, K. Ihm, H. Ahn, Y. Kang, H. S. Lee, D. Kim, Investigation of Thermally Induced Degradation in $CH_3NH_3PbI_3$ Perovskite Solar Cells using In-situ Synchrotron Radiation Analysis. *Sci. Rep.* **7**, 4645 (2017). doi:10.1038/s41598-017-04690-w Medline

17. C. C. Boyd, R. Cheacharoen, T. Leijtens, M. D. McGehee, Understanding Degradation Mechanisms and Improving Stability of Perovskite Photovoltaics. *Chem. Rev.* **119**, 3418–3451 (2019). doi:10.1021/acs.chemrev.8b00336 Medline

18. T. Leijtens, G. E. Eperon, S. Pathak, A. Abate, M. M. Lee, H. J. Snaith, Overcoming ultraviolet light instability of sensitized TiO_2 with meso-superstructured organometal tri-halide perovskite solar cells. *Nat. Commun.* **4**, 2885 (2013). doi:10.1038/ncomms3885 Medline

19. S. Ito, S. Tanaka, K. Manabe, H. Nishino, Effects of Surface Blocking Layer of Sb_2S_3 on Nanocrystalline TiO_2 for $CH_3NH_3PbI_3$ Perovskite Solar Cells. *J. Phys. Chem. C* **118**, 16995 (2014). doi:10.1021/jp500449z

20. J. Ahmad, K. Bazaka, L. J. Anderson, R. D. White, M. V. Jacob, Materials and methods for encapsulation of OPV: A review. *Renew. Sustain. Energy Rev.* **27**, 104–117 (2013). doi:10.1016/j.rser.2013.06.027

21. D. Yu, Y. Q. Yang, Z. Chen, Y. Tao, Y. F. Liu, Recent progress on thin-film encapsulation technologies for organic electronic devices. *Opt. Commun.* **362**, 43–49 (2016). doi:10.1016/j.optcom.2015.08.021

22. A. Uddin, M. Upama, H. Yi, L. Duan, Encapsulation of Organic and Perovskite Solar Cells: A Review. *Coatings* **9**, 65 (2019). doi:10.3390/coatings9020065

23. M. D. Kempe, A. A. Dameron, M. O. Reese, Evaluation of moisture ingress from the perimeter of photovoltaic modules. *Prog. Photovolt. Res. Appl.* **22**, 1159–1171 (2014). doi:10.1002/pip.2374

24. F. J. Pern, R. Noufi, paper presented at SPIE Optics + Photonics, San Diego, CA, 16 October 2012.

25. L. Shi, T. L. Young, J. Kim, Y. Sheng, L. Wang, Y. Chen, Z. Feng, M. J. Keevers, X. Hao, P. J. Verlinden, M. A. Green, A. W. Y. Ho-Baillie, Accelerated Lifetime Testing of Organic-Inorganic Perovskite Solar Cells Encapsulated by Polyisobutylene. *ACS Appl. Mater. Interfaces* **9**, 25073–25081 (2017). doi:10.1021/acsami.7b07625 Medline

26. F. Matteocci, L. Cinà, E. Lamanna, S. Cacovich, G. Divitini, P. A. Midgley, C. Ducati, A. Di Carlo, Encapsulation for long-term stability enhancement of perovskite solar cells. *Nano Energy* **30**, 162–172 (2016). doi:10.1016/j.nanoen.2016.09.041

27. Y. Han, S. Meyer, Y. Dkhissi, K. Weber, J. Pringle, U. Bach, L. Spiccia, Y.-B. Cheng, Degradation observations of encapsulated planar $CH_3NH_3PbI_3$ perovskite solar cells at high temperatures and humidity. *J. Mater. Chem. A* **3**, 8139–8147 (2015). doi:10.1039/C5TA00358J

28. H. C. Weerasinghe, D. Vak, B. Robotham, C. J. Fell, D. Jones, A. D. Scully, New barrier encapsulation and lifetime assessment of printed organic photovoltaic modules. *Sol. Energy Mater. Sol. Cells* **155**, 108–116 (2016). doi:10.1016/j.solmat.2016.04.051

29. Q. Dong, F. Liu, M. K. Wong, H. W. Tam, A. B. Djurišić, A. Ng, C. Surya, W. K. Chan, A. M. C. Ng, Encapsulation of Perovskite Solar Cells for High Humidity Conditions. *ChemSusChem* **9**, 2597–2603 (2016). doi:10.1002/cssc.201601090 Medline

30. J. Kim, N. Park, J. S. Yun, S. Huang, M. A. Green, A. W. Y. Ho-Baillie, An effective method of predicting perovskite solar cell lifetime–Case study on planar $CH_3NH_3PbI_3$ and $HC(NH_2)_2PbI_3$ perovskite solar cells and hole transfer materials of spiro-OMeTAD and PTAA. *Sol. Energy Mater. Sol. Cells* **162**, 41–46 (2017). doi:10.1016/j.solmat.2016.12.043

31. G. E. Eperon, S. D. Stranks, C. Menelaou, M. B. Johnston, L. M. Herz, H. J. Snaith, Formamidinium lead trihalide: A broadly tunable perovskite for efficient planar heterojunction solar cells. *Energy Environ. Sci.* **7**, 982 (2014). doi:10.1039/c3ee43822h

32. W. Tan, A. R. Bowring, A. C. Meng, M. D. McGehee, P. C. McIntyre, Thermal Stability of Mixed Cation Metal Halide Perovskites in Air. *ACS Appl. Mater. Interfaces* **10**, 5485–5491 (2018). doi:10.1021/acsami.7b15263 Medline

33. C. Yi, J. Luo, S. Meloni, A. Boziki, N. Ashari-Astani, C. Grätzel, S. M. Zakeeruddin, U. Röthlisberger, M. Grätzel, Entropic stabilization of mixed A-cation ABX_3 metal halide perovskites for high performance perovskite solar cells. *Energy Environ. Sci.* **9**, 656–662 (2016). doi:10.1039/C5EE03255E

34. M. Saliba, T. Matsui, K. Domanski, J. Y. Seo, A. Ummadisingu, S. M. Zakeeruddin, J. P. Correa-Baena, W. R. Tress, A. Abate, A. Hagfeldt, M. Grätzel, Incorporation of rubidium

cations into perovskite solar cells improves photovoltaic performance. *Science* **354**, 206–209 (2016). doi:10.1126/science.aah5557 Medline

35. G. Grancini, C. Roldán-Carmona, I. Zimmermann, E. Mosconi, X. Lee, D. Martineau, S. Narbey, F. Oswald, F. De Angelis, M. Graetzel, M. K. Nazeeruddin, One-Year stable perovskite solar cells by 2D/3D interface engineering. *Nat. Commun.* **8**, 15684 (2017). doi:10.1038/ncomms15684 Medline

36. N. Li, Z. Zhu, C. C. Chueh, H. Liu, B. Peng, A. Petrone, X. Li, L. Wang, A. K. Y. Jen, Mixed Cation $FA_xPEA_{1-x}PbI_3$ with Enhanced Phase and Ambient Stability toward High-Performance Perovskite Solar Cells. *Adv. Energy Mater.* **7**, 1601307 (2017). doi:10.1002/aenm.201601307

37. Z. Wang, Q. Lin, F. P. Chmiel, N. Sakai, L. M. Herz, H. J. Snaith, Efficient ambient-air-stable solar cells with 2D-3D heterostructured butylammonium-caesium-formamidinium lead halide perovskites. *Nat. Energy* **2**, 17135 (2017). doi:10.1038/nenergy.2017.135

38. H. Tsai, W. Nie, J.-C. Blancon, C. C. Stoumpos, R. Asadpour, B. Harutyunyan, A. J. Neukirch, R. Verduzco, J. J. Crochet, S. Tretiak, L. Pedesseau, J. Even, M. A. Alam, G. Gupta, J. Lou, P. M. Ajayan, M. J. Bedzyk, M. G. Kanatzidis, A. D. Mohite, High-efficiency two-dimensional Ruddlesden-Popper perovskite solar cells. *Nature* **536**, 312–316 (2016). doi:10.1038/nature18306 Medline

39. A. R. bin M. Yusoff, M. K. Nazeeruddin, Low-Dimensional Perovskites: From Synthesis to Stability in Perovskite Solar Cells. *Adv. Energy Mater.* **8**, 1702073 (2018). doi:10.1002/aenm.201702073

40. Y. C. Kim, T. Y. Yang, N. J. Jeon, J. Im, S. Jang, T. J. Shin, H. W. Shin, S. Kim, E. Lee, S. Kim, J. H. Noh, S. I. Seok, J. Seo, Engineering interface structures between lead halide perovskite and copper phthalocyanine for efficient and stable perovskite solar cells. *Energy Environ. Sci.* **10**, 2109–2116 (2017). doi:10.1039/C7EE01931A

41. Y. Chen, Z. Yang, S. Wang, X. Zheng, Y. Wu, N. Yuan, W. H. Zhang, S. F. Liu, Design of an Inorganic Mesoporous Hole-Transporting Layer for Highly Efficient and Stable Inverted Perovskite Solar Cells. *Adv. Mater.* **30**, 1805660 (2018). doi:10.1002/adma.201805660

42. N. Arora, M. I. Dar, A. Hinderhofer, N. Pellet, F. Schreiber, S. M. Zakeeruddin, M. Grätzel, Perovskite solar cells with CuSCN hole extraction layers yield stabilized efficiencies greater than 20. *Science* **358**, 768–771 (2017). doi:10.1126/science.aam5655 Medline

43. E. Bi, H. Chen, F. Xie, Y. Wu, W. Chen, Y. Su, A. Islam, M. Grätzel, X. Yang, L. Han, Diffusion engineering of ions and charge carriers for stable efficient perovskite solar cells. *Nat. Commun.* **8**, 15330 (2017). doi:10.1038/ncomms15330 Medline

44. H. Tan, A. Jain, O. Voznyy, X. Lan, F. P. García de Arquer, J. Z. Fan, R. Quintero-Bermudez, M. Yuan, B. Zhang, Y. Zhao, F. Fan, P. Li, L. N. Quan, Y. Zhao, Z.-H. Lu, Z.

Yang, S. Hoogland, E. H. Sargent, Efficient and stable solution-processed planar perovskite solar cells via contact passivation. *Science* **355**, 722–726 (2017). doi:10.1126/science.aai9081 Medline

45. M. Saliba, T. Matsui, J.-Y. Seo, K. Domanski, J.-P. Correa-Baena, M. K. Nazeeruddin, S. M. Zakeeruddin, W. Tress, A. Abate, A. Hagfeldt, M. Grätzel, Cesium-containing triple cation perovskite solar cells: Improved stability, reproducibility and high efficiency. *Energy Environ. Sci.* **9**, 1989–1997 (2016). doi:10.1039/C5EE03874J Medline

46. K. A. Bush, A. F. Palmstrom, Z. J. Yu, M. Boccard, R. Cheacharoen, J. P. Mailoa, D. P. McMeekin, R. L. Z. Hoye, C. D. Bailie, T. Leijtens, I. M. Peters, M. C. Minichetti, N. Rolston, R. Prasanna, S. Sofia, D. Harwood, W. Ma, F. Moghadam, H. J. Snaith, T. Buonassisi, Z. C. Holman, S. F. Bent, M. D. McGehee, 23.6%-efficient monolithic perovskite/silicon tandem solar cells with improved stability. *Nat. Energy* **2**, 17009 (2017). doi:10.1038/nenergy.2017.9

47. S. Seo, S. Jeong, C. Bae, N. G. Park, H. Shin, Perovskite Solar Cells with Inorganic Electron- and Hole-Transport Layers Exhibiting Long-Term (≈500 h) Stability at 85°C under Continuous 1 Sun Illumination in Ambient Air. *Adv. Mater.* **30**, e1801010 (2018). doi:10.1002/adma.201801010 Medline

48. K. A. Bush, C. D. Bailie, Y. Chen, A. R. Bowring, W. Wang, W. Ma, T. Leijtens, F. Moghadam, M. D. McGehee, Thermal and Environmental Stability of Semi-Transparent Perovskite Solar Cells for Tandems Enabled by a Solution-Processed Nanoparticle Buffer Layer and Sputtered ITO Electrode. *Adv. Mater.* **28**, 3937–3943 (2016). doi:10.1002/adma.201505279 Medline

49. C. C. Boyd, R. Cheacharoen, K. A. Bush, R. Prasanna, T. Leijtens, M. D. McGehee, Barrier Design to Prevent Metal-Induced Degradation and Improve Thermal Stability in Perovskite Solar Cells. *ACS Energy Lett.* **3**, 1772–1778 (2018). doi:10.1021/acsenergylett.8b00926

50. Y. I. Lee, N. J. Jeon, B. J. Kim, H. Shim, T. Y. Yang, S. I. Seok, J. Seo, S. G. Im, A Low-Temperature Thin-Film Encapsulation for Enhanced Stability of a Highly Efficient Perovskite Solar Cell. *Adv. Energy Mater.* **8**, 1701928 (2018). doi:10.1002/aenm.201701928

51. K. O. Brinkmann, J. Zhao, N. Pourdavoud, T. Becker, T. Hu, S. Olthof, K. Meerholz, L. Hoffmann, T. Gahlmann, R. Heiderhoff, M. F. Oszajca, N. A. Luechinger, D. Rogalla, Y. Chen, B. Cheng, T. Riedl, Suppressed decomposition of organometal halide perovskites by impermeable electron-extraction layers in inverted solar cells. *Nat. Commun.* **8**, 13938 (2017). doi:10.1038/ncomms13938 Medline

52. R. Cheacharoen, C. C. Boyd, G. Burkhard, T. Leijtens, J. Raiford, K. A. Bush, S. Bent, M. D. McGehee, Encapsulating perovskite solar cells to withstand damp heat and thermal cycling. *Sustain. Energy Fuels* **2**, 2398–2406 (2018). doi:10.1039/C8SE00250A

53. Z. Li, M. Yang, J. S. Park, S. H. Wei, J. J. Berry, K. Zhu, Stabilizing Perovskite Structures by Tuning Tolerance Factor: Formation of Formamidinium and Cesium Lead Iodide Solid-State Alloys. *Chem. Mater.* **28**, 284–292 (2016). doi:10.1021/acs.chemmater.5b04107

54. A. Dualeh, P. Gao, S. I. Seok, M. K. Nazeeruddin, M. Gratzel, Thermal Behavior of Methylammonium Lead-trihalide Perovskite Photovoltaic Light Harvesters. *Chem. Mater.* **26**, 6160–6164 (2014). doi:10.1021/cm502468k

55. D. P. Nenon, J. A. Christians, L. M. Wheeler, J. L. Blackburn, E. M. Sanehira, B. Dou, M. L. Olsen, K. Zhu, J. J. Berry, J. M. Luther, Structural and chemical evolution of methylammonium lead halide perovskites during thermal processing from solution. *Energy Environ. Sci.* **9**, 2072–2082 (2016). doi:10.1039/C6EE01047D

56. A. E. Williams, P. J. Holliman, M. J. Carnie, M. L. Davies, D. A. Worsley, T. M. Watson, Perovskite processing for photovoltaics: A spectro-thermal evaluation. *J. Mater. Chem. A* **2**, 19338–19346 (2014). doi:10.1039/C4TA04725G

57. L. Ma, D. Guo, M. Li, C. Wang, Z. Zhou, X. Zhao, F. Zhang, Z. Ao, Z. Nie, Temperature-dependent thermal decomposition pathway of organic-inorganic halide perovskite materials. *Chem. Mater.* **31**, 8515–8522 (2019). doi:10.1021/acs.chemmater.9b03190

58. E. J. Juarez-Perez, Z. Hawash, S. R. Raga, L. K. Ono, Y. Qi, Thermal degradation of $CH_3NH_3PbI_3$ perovskite into NH_3 and CH_3I gases observed by coupled thermogravimetry-mass spectrometry analysis. *Energy Environ. Sci.* **9**, 3406–3410 (2016). doi:10.1039/C6EE02016J

59. E. J. Juarez-Perez, L. K. Ono, M. Maeda, Y. Jiang, Z. Hawash, Y. Qi, Photodecomposition and thermal decomposition in methylammonium halide lead perovskites and inferred design principles to increase photovoltaic device stability. *J. Mater. Chem. A* **6**, 9604–9612 (2018). doi:10.1039/C8TA03501F

60. Z. Fan, H. Xiao, Y. Wang, Z. Zhao, Z. Lin, H. C. Cheng, S. J. Lee, G. Wang, Z. Feng, W. A. Goddard III, Y. Huang, X. Duan, Layer-by-Layer Degradation of Methylammonium Lead Tri-iodide Perovskite Microplates. *Joule* **1**, 548–562 (2017). doi:10.1016/j.joule.2017.08.005

61. E. J. Juarez-Perez, L. K. Ono, I. Uriarte, E. J. Cocinero, Y. Qi, Degradation Mechanism and Relative Stability of Methylammonium Halide Based Perovskites Analyzed on the Basis of Acid-Base Theory. *ACS Appl. Mater. Interfaces* **11**, 12586–12593 (2019). doi:10.1021/acsami.9b02374 Medline

62. International Electrotechnical Commission, *Terrestrial photovoltaic (PV) modules - Design qualification and type approval - Part 1: Test requirements*; https://webstore.iec.ch/publication/24312.

63. A. Latini, G. Gigli, A. Ciccioli, A study on the nature of the thermal decomposition of methylammonium lead iodide perovskite, $CH_3NH_3PbI_3$: An attempt to rationalise contradictory experimental results. *Sustain. Energy Fuels* **1**, 1351–1357 (2017). doi:10.1039/C7SE00114B

64. E. J. Juarez-Perez, L. K. Ono, Y. Qi, Thermal degradation of formamidinium based lead halide perovskites into sym-triazine and hydrogen cyanide observed by coupled thermogravimetry - mass spectrometry analysis. *J. Mater. Chem. A* **7**, 16912–16919 (2019). doi:10.1039/C9TA06058H

65. I. L. Ivanov, A. S. Steparuk, M. S. Bolyachkina, D. S. Tsvetkov, A. P. Safronov, A. Y. Zuev, Thermodynamics of formation of hybrid perovskite-type methylammonium lead halides. *J. Chem. Thermodyn.* **116**, 253–258 (2018). doi:10.1016/j.jct.2017.09.026

66. J. Speight, *Lange's Handbook of Chemistry* (McGraw-Hill, ed. 16, 2005); https://www.accessengineeringlibrary.com/content/book/9780071432207/toc-chapter/chapter1/section/section83.

67. NIST Chemistry WebBook; https://webbook.nist.gov/chemistry/.

68. H. Bipp, H. Kieczka, Formamides. In *Ullmann's Encyclopedia of Industrial Chemistry* (Wiley-VCH, ed. 7, 2011), vol. 16.

69. A. F. Akbulatov, L. A. Frolova, N. N. Dremova, I. Zhidkov, V. M. Martynenko, S. A. Tsarev, S. Y. Luchkin, E. Z. Kurmaev, S. M. Aldoshin, K. J. Stevenson, P. A. Troshin, Light or Heat: What Is Killing Lead Halide Perovskites under Solar Cell Operation Conditions? *J. Phys. Chem. Lett.* **11**, 333–339 (2020). doi:10.1021/acs.jpclett.9b03308 Medline

70. B. A. Turowec, E. R. Gillies, Synthesis, properties and degradation of polyisobutylene–polyester graft copolymers. *Polym. Int.* **66**, 42–51 (2017). doi:10.1002/pi.5250

71. R. Cheacharoen, N. Rolston, D. Harwood, K. A. Bush, R. H. Dauskardt, M. D. McGehee, Design and understanding of encapsulated perovskite solar cells to withstand temperature cycling. *Energy Environ. Sci.* **11**, 144–150 (2018). doi:10.1039/C7EE02564E

72. Gas Chromatography Problem Solving and Troubleshooting. *J. Chromatogr. Sci.* **37**, 313 (1999). doi:10.1093/chromsci/37.8.313

73. M. Zhang, B. Wilkinson, Y. Liao, J. Zheng, C. F. J. Lau, J. Kim, J. Bing, M. A. Green, S. Huang, A. W.-Y. Ho-Baillie, Electrode Design to Overcome Substrate Transparency Limitations for Highly Efficient 1 cm^2 Mesoscopic Perovskite Solar Cells. *Joule* **2**, 2694–2705 (2018). doi:10.1016/j.joule.2018.08.012

74. R. B. Dunbar, B. C. Duck, T. Moriarty, K. F. Anderson, N. W. Duffy, C. J. Fell, J. Kim, A. Ho-Baillie, D. Vak, T. Duong, Y. Wu, K. Weber, A. Pascoe, Y.-B. Cheng, Q. Lin, P. L. Burn, R. Bhattacharjee, H. Wang, G. J. Wilson, How reliable are efficiency measurements of perovskite solar cells? The first inter-comparison, between two accredited and eight non-accredited laboratories. *J. Mater. Chem. A* **5**, 22542–22558 (2017). doi:10.1039/C7TA05609E

75. S. Liu, W. Huang, P. Liao, N. Pootrakulchote, H. Li, J. Lu, J. Li, F. Huang, X. Shai, X. Zhao, Y. Shen, Y. B. Cheng, M. Wang, 17% efficient printable mesoscopic PIN metal oxide framework perovskite solar cells using cesium-containing triple cation perovskite. *J. Mater. Chem. A* **5**, 22952–22958 (2017). doi:10.1039/C7TA07660F

76. M. B. Islam, M. Yanagida, Y. Shirai, Y. Nabetani, K. Miyano, NiO_x Hole Transport Layer for Perovskite Solar Cells with Improved Stability and Reproducibility. *ACS Omega* **2**, 2291–2299 (2017). doi:10.1021/acsomega.7b00538 Medline

77. Y. Wu, P. Wang, S. Wang, Z. Wang, B. Cai, X. Zheng, Y. Chen, N. Yuan, J. Ding, W. H. Zhang, Heterojunction Engineering for High Efficiency Cesium Formamidinium Double-Cation Lead Halide Perovskite Solar Cells. *ChemSusChem* **11**, 837–842 (2018). doi:10.1002/cssc.201702221 Medline

78. Q. Jiang, Y. Zhao, X. Zhang, X. Yang, Y. Chen, Z. Chu, Q. Ye, X. Li, Z. Yin, J. You, Surface passivation of perovskite film for efficient solar cells. *Nat. Photonics* **13**, 460–466 (2019). doi:10.1038/s41566-019-0398-2